Hermann Ulrich Schnait, BSc

Interplay of spin-orbit coupling and electronic correlations in Iridium double perovskites

MASTER'S THESIS

to achieve the university degree of

Diplom-Ingenieur

Master's degree programme: Technical Physics

submitted to

Graz University of Technology

Supervisor

Assoc.Prof. Dipl.-Ing. Dr.techn. Markus Aichhorn

Institute of Theoretical and Computational Physics

Graz, March 2019

AFFIDAVIT

I declare that I have authored this thesis independently, that I have not used other than the declared sources/resources, and that I have explicitly indicated all material which has been quoted either literally or by content from the sources used. The text document uploaded to TUGRAZonline is identical to the present master‘s thesis.

Date

Signature

Abstract

The double-perovskite transition-metal oxide Ba_2YIrO_6 (electronic configuration $5d^4$) shows fascinating magnetic properties which cannot be explained by simple atomic-picture Hund's rules. In this material, the ground-state properties are driven by a delicate interplay between spin-orbit coupling and electronic correlations under a strong cubic crystal-field. There is yet no scientific consensus as why its magnetic state is realized and whether long-range magnetic ordering occurs for this material.

In this work, the electronic and magnetic properties of Ba_2YIrO_6 were investigated using a combination of density-functional theory (DFT) and dynamic mean-field theory (DMFT). The calculations were performed both for the paramagnetic phase as well as for a Type I (fcc) anti-ferromagnetic phase. In the paramagnetic phase a clear breakdown of the atomic $J_{\text{eff}} = 0$ state was observed. This effect is driven by a combination of low-enough spin-orbit coupling and large-enough bandwidth, leading to an overlap of the $J_{\text{eff}} = 1/2$ and $J_{\text{eff}} = 3/2$ orbitals before the Mott transition. After the Mott transition, the lower Hubbard band of the $J_{\text{eff}} = 1/2$ orbital lies below the Fermi energy and thus a magnetic moment is present. In our calculations for a possible anti-ferromagnetic phase no long-range ordering was observed down to 100 K. The used QMC solver limited the investigation of lower temperatures and a different solver needs to be employed to make a convincing argument for or against long-range ordering.

Kurzfassung

Das Doppelperowskit-Übergangsmetalloxid Ba_2YIrO_6 (Elektronenkonfiguration $5d^4$) zeigt faszinierende magnetische Eigenschaften, die sich nicht durch die einfachen Hund'schen Regeln erklären lassen. In diesem Material werden die physikalischen Eigenschaften durch ein empfindliches Zusammenspiel von Spin-Orbit-Kopplung und elektronischen Korrelationen unter einer starken kubischen Kristallfeldaufspaltung bestimmt. Es gibt noch keinen wissenschaftlichen Konsens darüber, warum in diesem Material ein magnetischer Zustand realisiert wird und ob für dieses Material eine weitreichende magnetische Ordnung vorliegt.

In dieser Arbeit wurden die elektronischen und magnetischen Eigenschaften von Ba_2YIrO_6 mit einer Kombination aus Dichtefunktionaltheorie (DFT) und dynamischer Molekularfeld-Theorie (DMFT) untersucht. Die Berechnungen wurden sowohl für die paramagnetische Phase als auch für eine antiferromagnetische Phase des Typs I (fcc) durchgeführt. In der paramagnetischen Phase wurde ein deutlicher Zusammenbruch des $J_{\text{eff}} = 0$ Zustandes beobachtet. Dieser Effekt wird durch eine Kombination aus einer genügend schwachen Spin-Orbit-Kopplung und einer ausreichend großen Bandbreite ausgelöst, was zu einer Überlappung der $J_{\text{eff}} = 1/2$ und $J_{\text{eff}} = 3/2$ Orbitale vor dem Mott-Übergang führt. Nach dem Mott-Übergang liegt das untere Hubbard-Band des $J_{\text{eff}} = 1/2$ Orbitals unterhalb der Fermi-Energie, womit ein magnetisches Moment vorhanden ist. In unseren Berechnungen für eine mögliche antiferromagnetische Phase wurde keine magnetische Ordnung bis zu 100 K beobachtet. Der verwendete QMC-Solver schränkte die Untersuchung niedrigerer Temperaturen ein und es muss ein anderer Solver eingesetzt werden, um ein überzeugendes Argument für oder gegen eine magnetische Ordnung zu liefern.

Contents

1 Introduction 1
1.1 Strongly Correlated Materials 1
1.1.1 Strong correlations and SOC 1
1.2 Double perovskite Iridates - Ba_2YIrO_6 2

2 Theoretical foundations 5
2.1 Basics 5
2.1.1 Crystal field splitting 6
2.1.2 Spin-orbit coupling 10
2.1.3 Ordered spin structures 14
2.1.4 Green's functions 16
2.2 Band structure calculations 17
2.2.1 DFT 17
2.2.2 DMFT 21
2.2.3 DFT+DMFT 29

3 Implementation Details 33
3.1 Used code packages 33
3.1.1 Wien2k 33
3.1.2 dmftproj 34
3.1.3 TRIQS 34
3.2 DMFT in TRIQS 36
3.2.1 From dmftproj to TRIQS 36
3.2.2 Basis transformations 37
3.2.3 "Hermitian Symmetrization" of Sigma 41
3.2.4 DMFT Loop 43
3.2.5 Observables and expectation values 44
3.2.6 AFM calculations 48

4 Application to $\mathbf{Ba_2YIrO_6}$ 51
4.1 Paramagnetic System 51
4.1.1 Structure 51
4.1.2 DFT + dmftproj 51
4.1.3 DMFT 56
4.2 Antiferromagnetic System 63
4.2.1 Structure 63
4.2.2 DFT 63
4.2.3 DMFT 64
4.3 Summary and Outlook 66

Chapter 1

Introduction

1.1 Strongly Correlated Materials

Strongly correlated materials are a fascinating topic in modern solid state physics. In this class of materials, the electrons cannot be seen as non-interacting any more, leading to interesting physical phenomena such as Mott-Insulator transitions [1], charge- and spin-density wave physics [2] and high T_c superconductivity [3]. As electron-electron interactions drive these phenomena, it usually is not sufficient to describe the system in a simple mean field approach (such as DFT) and one has to switch to more sophisticated methods (e.g. DMFT) which include quantum many-body effects.

One vast playground to investigate these phenomena are transition-metals and their oxides, with their strongly localized $3d$, $4d$ and $5d$ electron orbitals. For many of these TMOs a density-based approach in the context of DFT results in a metallic behavior. However, upon introducing a Coulomb repulsion between the electrons in the form of a interaction-parameter U, the DOS at the Fermi energy splits up into two Hubbard bands, rendering the system insulating.

1.1.1 Strong correlations and SOC

For a long time $5d$ materials were considered weakly correlated, as their spatially more extended orbitals would lead to a lower interaction parameter U, pushing them out of the Mott-insulating region of $U \approx W$ (W being the bandwidth) [4]. It was shown by Kim *et al.* [4], that including spin-orbit coupling (SOC) for Sr_2IrO_4 ($5d^5$) the t_{2g} band is split into a fully filled $J_{\text{eff}} = 3/2$ and a half-filled $J_{\text{eff}} = 1/2$ band. The $J_{\text{eff}} = 1/2$ band is then split into two Hubbard bands, creating a $J_{\text{eff}} = 1/2$ Mott-insulator.

Taking the same approach for $5d^4$ systems, one would expect a non-magnetic $J_{\text{eff}} = 0$ ground state with fully filled $J_{\text{eff}} = 3/2$ orbitals and empty $J_{\text{eff}} = 1/2$ orbitals. While this non-magnetic state is realized in NaIrO_3 [5,6,7], we will see in section 1.2 that this is apparently not the case for Ba_2YIrO_6. The cause of this shall be investigated in this thesis and will be discussed in section 4.

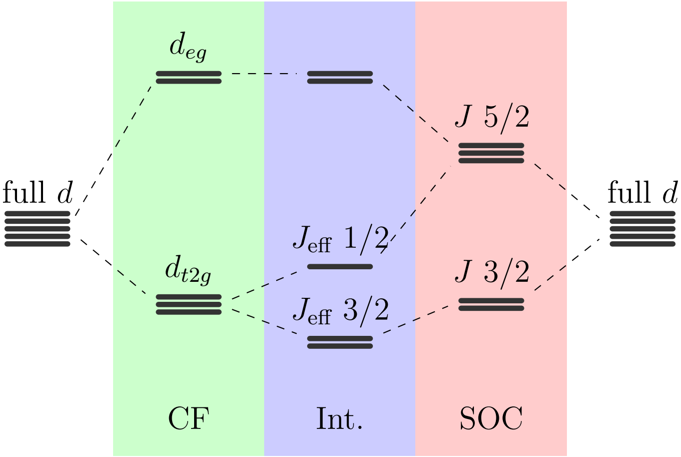

Figure 1.1 – Energy splittings of d-orbitals under spin-orbit coupling (SOC) and crystal field (CF). For the material considered in this work, we find ourselves in the intermediate region (Int.). [4]

1.2 Double perovskite Iridates - Ba_2YIrO_6

Soon after unexpected magnetic behaviour was first observed in Sr_2YIrO_6 [8], research also focused on Ba_2YIrO_6 (BYIO) with its distortion-free crystal structure (see Fig. 1.2). BYIO crystalizes in a cubic double perovskite structue [5, 9] without any tilting of the oxygen octahedra and an electron configuration of $5d^4$. This double perovskite structure with large Ir-Ir distances of 5.9 Å [9] and the corresponding small Ir-Ir exchange interaction together with the increased SOC due to a strict cubic symmetry was thought to lead to a non-magnetic ground state [10].

Surprisingly, different experimental [5,10,11] and theoretical [12,13] studies showed that BYIO exhibits an exotic magnetic ground state with $J_{\text{eff}} \neq 0$. However, the explanations as why this happens are ambiguous. While Fuchs *et al.* [14] attribute their observed magnetism solely on Ir^{4+} and Ir^{6+} defects within non-magnetic Ir^{5+} sites, the other publications cited above claim an observation of magnetism even for the Ir^{5+} ions (e.g. Dey *et al.* [5] observed magnetism even after annealing their sample under 700 bar oxygen at 500 °C for 2 days).

Terzic *et al.* [11] laid out three possible explanations for the stabilization of the magnetic moment in Ir^{5+}: (1) Overlap of the $J_{\mathrm{eff}} = 1/2$ and $J_{\mathrm{eff}} = 3/2$ bands caused by an increase in bandwidth due to hopping. (2) Excitonic magnetism [15, 16]. (3) Band structure effects [8].

Pajskr *et al.* [12] suspect orbitally polarized and gapped bands rather than excitons to be responsible for the magnetic ground state.

It is also unclear whether BYIO undergoes a phase transition into an ordered state at low temperatures. While Terzic *et al.* [11] observed long-range magnetic ordering below 1.7 K, Dey *et al.* [5] claim an absence of long-range magnetic order down to 0.4 K.

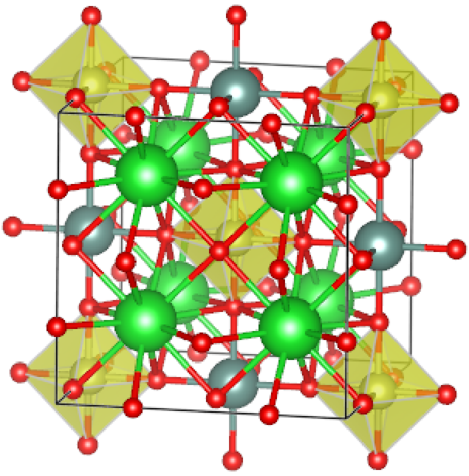

Figure 1.2 – Double perovskite crystal structure of Ba_2YIrO_6.
In green the Ba atoms, grey the Y atoms, red the O atoms and yellow the Ir atoms with their oxygen-octahedra are shown.

Chapter 2

Theoretical foundations

2.1 Basics

In solid state physics, we are primarily interested in solving the Schroedinger equation for atoms in a crystal lattice. This means, if we can diagonalize the system's Hamiltonian, we can find all the interesting physics of the system.

The non-relativistic Hamiltonian for a system consisting of nuclei (greek indices and captial coordinates $\boldsymbol{R}_\alpha$, nuclear charges Z_α) and electrons (latin indices and small coordinates $\boldsymbol{r}_i$) can be formally written down as ($\hbar = 1$):

$$\begin{aligned} H = -\frac{1}{2}\sum_i \nabla_i^2 - \frac{1}{2}\sum_\alpha \frac{1}{m_\alpha}\nabla_\alpha^2 + \frac{1}{2}\sum_{ij,i\neq j}\frac{1}{|\boldsymbol{r}_i - \boldsymbol{r}_j|} + \\ + \frac{1}{2}\sum_{\alpha\beta,\alpha\neq\beta}\frac{Z_\alpha Z_\beta}{|\boldsymbol{R}_\alpha - \boldsymbol{R}_\beta|} - \sum_{i\alpha}\frac{Z_\alpha}{|\boldsymbol{r}_i - \boldsymbol{R}_\alpha|} \end{aligned} \tag{2.1}$$

However, equation (2.1) is impossible to solve for all real systems apart from the Hydrogen atom. To tackle this problem, one usually starts by taking the Born-Oppenheimer approximation, thus decoupling the movement of electrons and nuclei. For the relevant energy scale in solid state physics, we can neglect the dynamics of the nuclei and concentrate on the electrons moving in the Coulomb potential created by the nuclei (the crystal potential $v_c(\boldsymbol{r})$):

$$H_{BO} = -\frac{1}{2}\sum_i \nabla_i^2 + \frac{1}{2}\sum_{ij,i\neq j}\frac{1}{|\boldsymbol{r}_i - \boldsymbol{r}_j|} - \underbrace{\sum_{i\alpha}\frac{Z_\alpha}{|\boldsymbol{r}_i - \boldsymbol{R}_\alpha|}}_{\sum_i v_c(\boldsymbol{r}_i)} \tag{2.2}$$

Still, the electron-electron interaction term (the second term in equation (2.2)) remains problematic. To avoid this problem, one option is to re-

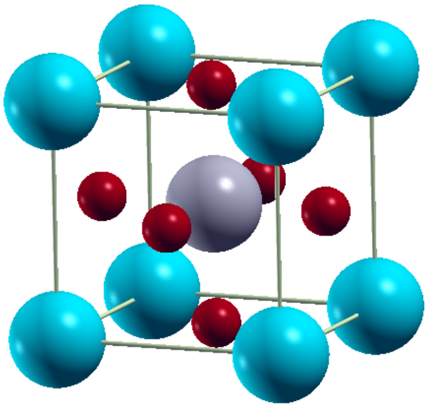

Figure 2.1 – Perovskite crystal structure
In grey the transition metal ion, in red the oxygen octahedron, in blue the other positive ions are shown.

place the many-body electron-electron interaction by an effective one-particle potential in the scope of Density Functional Theory (DFT).

DFT will be introduced in section 2.2.1, in the following section 2.1.1 we will first look at crystal symmetry effects (symmetries in $v_c(\boldsymbol{r})$) on the resulting wave functions, and then in section 2.1.2 derive the relativistic spin-orbit terms.

2.1.1 Crystal field splitting

As an atom is rotationally symmetric, all atomic electron wave functions have to be rotationally invariant. Of course this is no longer valid when considering electrons in a crystal. Depending on the crystal structure, the symmetry will be lower, which can lead to splitting of originally degenerated energy levels.

2.1.1.1 Crystal field splitting of d-orbitals in octahedral symmetry

In perovskite and double perovskite transition metal oxides, the (positivly charged) transition metal ion sits inside an octahedron of surrounding (negative) oxygen atoms and inside a cubic cage of other positive ions (see Fig. 2.1).

We can model the Coulomb potential acting on the electrons of the transition metal ion as

$$v_c(\boldsymbol{r}) = \sum_i \frac{q_i}{|\boldsymbol{R}_i - \boldsymbol{r}|} \tag{2.3}$$

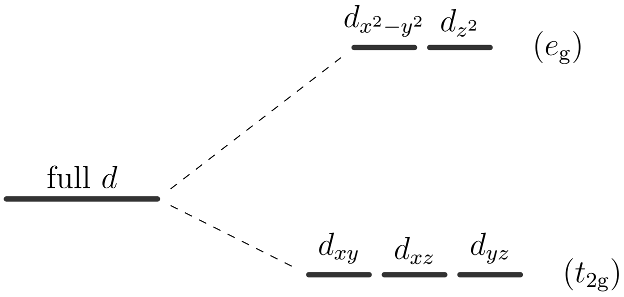

Figure 2.2 – Crystal-field splitting of d orbitals under octahedral crystal field

The octahedral oxygen atoms (with charge q_o) are located at $(\pm a, 0, 0)$, $(0, \pm a, 0)$ and $(0, 0, \pm a)$ (with a being half the lattice constant). Expanding equation (2.3) around $\boldsymbol{r} = 0$ leads in first order to [17]

$$v_{oct}(\boldsymbol{r}) = \frac{35q_o}{4a^5}(x^4 + y^4 + z^4 - \frac{3}{5}r^4) \tag{2.4}$$

Doing the same for the cubic cage of ions at $(\pm a, \pm a, \pm a)$ leads to a similar result

$$v_{cub}(\boldsymbol{r}) = -\frac{8}{9}\frac{q_{ion}}{q_o}v_{oct}(\boldsymbol{r}) \tag{2.5}$$

However, $q_{ion}/q_o < 0$ as the ionic cage is positivly charged. Thus, the ionic cage has the same effect as the octahedral oxygen atoms surrounding our transition metal ion.

The derivation of the actual form of the splitting can be found e.g. in [17]. As a deep dive into the required group theoretical basics for this derivation would be too much for the scope of this work, we will just look at the well-known result [17]:

$$\Gamma^d = e \oplus t_2 \tag{2.6}$$

Thus the d orbitals split up into a threefold degenerate t_{2g} and a twofold degenerate e_g manifold. It can be further shown [17] that the e_g orbitals lie higher in energy, which makes sense as they point towards the negativly charged oxygen atoms and thus should have a higher Coulomb repulsion. An orbital diagram showing this behaviour can be found in Fig. 2.2.

2.1.1.2 Angular momentum and T-P equivalence

Taking the crystal-field splitting between the e_g and t_{2g} orbitals into consideration, one can find an interesting effect on the angular momentum operators of the d orbitals.

The angular momentum operators are defined as [18]

$$\begin{aligned} &L_z \left|l, m_l\right\rangle = \hbar m_l \left|l, m_l\right\rangle \\ &L_\pm \left|l, m_l\right\rangle = \hbar\sqrt{l(l+1) - m_l(m_l \pm 1)}\left|l, m_l \pm 1\right\rangle \\ &\text{ with } L_\pm = L_x \pm iL_y \end{aligned} \tag{2.7}$$

With the convention $\hbar = 1$, this leads to the following matrix representations in the spherical basis for p $(l = 1)$ and d $(l = 2)$ orbitals:

$$L_x^{\text{p, sph}} = \frac{1}{\sqrt{2}}\begin{bmatrix} 0 & 1 & 0 \\ 1 & 0 & 1 \\ 0 & 1 & 0 \end{bmatrix} \quad L_y^{\text{p, sph}} = \frac{1}{\sqrt{2}}\begin{bmatrix} 0 & i & 0 \\ -i & 0 & i \\ 0 & -i & 0 \end{bmatrix}$$

$$L_z^{\text{p, sph}} = \begin{bmatrix} -1 & 0 & 0 \\ 0 & 0 & 0 \\ 0 & 0 & 1 \end{bmatrix} \tag{2.8}$$

$$\begin{aligned} L_x^{\text{d, sph}} &= \begin{bmatrix} 0 & 1 & 0 & 0 & 0 \\ 1 & 0 & \sqrt{3/2} & 0 & 0 \\ 0 & \sqrt{3/2} & 0 & \sqrt{3/2} & 0 \\ 0 & 0 & \sqrt{3/2} & 0 & 1 \\ 0 & 0 & 0 & 1 & 0 \end{bmatrix} \\ L_y^{\text{d, sph}} &= i\begin{bmatrix} 0 & -1 & 0 & 0 & 0 \\ 1 & 0 & -\sqrt{3/2} & 0 & 0 \\ 0 & \sqrt{3/2} & 0 & -\sqrt{3/2} & 0 \\ 0 & 0 & \sqrt{3/2} & 0 & -1 \\ 0 & 0 & 0 & 1 & 0 \end{bmatrix} \\ L_z^{\text{d, sph}} &= \begin{bmatrix} -2 & 0 & 0 & 0 & 0 \\ 0 & -1 & 0 & 0 & 0 \\ 0 & 0 & 0 & 0 & 0 \\ 0 & 0 & 0 & 1 & 0 \\ 0 & 0 & 0 & 0 & 2 \end{bmatrix} \end{aligned} \tag{2.9}$$

We will define a convention for basis transformations more rigorously in section 3.2.2. For now we take for any matrix M (in basis $\mathcal{A}$ or $\mathcal{B}$):

$$M^{\mathcal{B}} = (T_{\mathcal{A}\to\mathcal{B}})M^{\mathcal{A}}(T_{\mathcal{A}\to\mathcal{B}})^\dagger \tag{2.10}$$

We then introduce a cubic basis for the d orbitals with the following transformation matrix[1]:

$$T^{l=2}_{\text{sph}\to\text{cub}} = \begin{bmatrix} 0 & 0 & 1 & 0 & 0 \\ 1/\sqrt{2} & 0 & 0 & 0 & 1/\sqrt{2} \\ -1/\sqrt{2} & 0 & 0 & 0 & 1/\sqrt{2} \\ 0 & 1/\sqrt{2} & 0 & -1/\sqrt{2} & 0 \\ 0 & 1/\sqrt{2} & 0 & 1/\sqrt{2} & 0 \end{bmatrix} \tag{2.11}$$

Transforming the spherical L^{d} matrices (2.9) to this cubic basis leads to the L^{d} matrices in cubic basis (the horizontal and vertical lines separating the e_{g} and $t_{2\text{g}}$ blocks):

$$\begin{aligned} L_x^{\text{d, cub}} &= \left[\begin{array}{cc|ccc} 0 & 0 & 0 & 0 & \sqrt{3} \\ 0 & 0 & 0 & 0 & 1 \\ \hline 0 & 0 & 0 & -1 & 0 \\ 0 & 0 & -1 & 0 & 0 \\ \sqrt{3} & 1 & 0 & 0 & 0 \end{array}\right] \\ L_y^{\text{d, cub}} &= i \left[\begin{array}{cc|ccc} 0 & 0 & 0 & -\sqrt{3} & 0 \\ 0 & 0 & 0 & 1 & 0 \\ \hline 0 & 0 & 0 & 0 & -1 \\ \sqrt{3} & -1 & 0 & 0 & 0 \\ 0 & 0 & 1 & 0 & 0 \end{array}\right] \\ L_z^{\text{d, cub}} &= \left[\begin{array}{cc|ccc} 0 & 0 & 0 & 0 & 0 \\ 0 & 0 & 2 & 0 & 0 \\ \hline 0 & 2 & 0 & 0 & 0 \\ 0 & 0 & 0 & 0 & -1 \\ 0 & 0 & 0 & -1 & 0 \end{array}\right] \end{aligned} \tag{2.12}$$

Under strong crystal fields one can assume the e_{g} and $t_{2\text{g}}$ blocks to be decoupled. As the e_{g} block has no entries in the $\boldsymbol{L}$ matrices, the spin orbit coupling $\boldsymbol{L}\cdot\boldsymbol{S}$ has no effect on these orbitals in this approximation (see section 2.1.2.2).

We can further look at the L^{p} matrices under a transformation to the cubic basis[2]:

$$T^{l=1}_{\text{sph}\to\text{cub}} = \begin{bmatrix} 0 & 1 & 0 \\ 1/\sqrt{2} & 0 & 1/\sqrt{2} \\ -1/\sqrt{2} & 0 & 1/\sqrt{2} \end{bmatrix} \tag{2.13}$$

---

[1] This is the convention used in Wien2k and dmftproj.

[2] Same as for the $l = 2$ cubic harmonics, there are many different ways to define these transformations. Using this real valued transformation matrix leads to the T-P equivalence for the real valued $T^{l=2}$ (2.11) used by Wien2k.

Transforming the $L^{\mathrm{p,\,sph}}$ from (2.8), we get:

$$L_x^{\mathrm{p,\,cub}} = \begin{bmatrix} 0 & 1 & 0 \\ 1 & 0 & 0 \\ 0 & 0 & 0 \end{bmatrix} \quad L_y^{\mathrm{p,\,cub}} = i \begin{bmatrix} 0 & 0 & 1 \\ 0 & 0 & 0 \\ -1 & 0 & 0 \end{bmatrix} \quad L_z^{\mathrm{p,\,cub}} = \begin{bmatrix} 0 & 0 & 0 \\ 0 & 0 & 1 \\ 0 & 1 & 0 \end{bmatrix} \tag{2.14}$$

Comparing the matrices in (2.12) and (2.14), it can be seen that the part of the L^{d} operator acting on the $t_{2\mathrm{g}}$ block is equal to the negative L^{p} operator. This is called the T-P equivalence, and is often written as

$$\boldsymbol{L}(t_{2\mathrm{g}}) = -\boldsymbol{L}(p) \tag{2.15}$$

This means the $t_{2\mathrm{g}}$ orbitals have an effective angular momentum of $l_{\mathrm{eff}} = 1$ due to the quenching of the e_{g} orbitals.

2.1.2 Spin-orbit coupling

The effect of the spin-orbit coupling has a relativistic origin, which we will derive in section 2.1.2.1. However, even from a semi-classical picture of an electron moving in a circular orbit around a positivly charged nucleus, an almost correct term can be derived.

As the (semi-classical) electron moves in the electric field of the nucleus, it experiences a magnetic field:

$$\boldsymbol{B} = -(\boldsymbol{v} \times \boldsymbol{E})/c^2 \tag{2.16}$$

With the electron having an intrinsic magnetic moment[3] $\boldsymbol{\mu} = -e/m_e\ \boldsymbol{s}$, the interaction with the magnetic field $\boldsymbol{B}$ leads to an energy shift ΔE:

$$\Delta E = -\boldsymbol{\mu} \cdot \boldsymbol{B} = -\frac{e}{m_e c^2} \boldsymbol{s} \cdot (\boldsymbol{v} \times \boldsymbol{E}) = \frac{e}{m_e^2 c^2} \boldsymbol{s} \cdot (\boldsymbol{E} \times \boldsymbol{p}) \tag{2.17}$$

Using the radial symmetry of the nucleus' electric field $\boldsymbol{E} = -\nabla\phi(r) = \frac{\boldsymbol{r}}{r}\frac{\partial\phi}{\partial r}$ equation (2.17) can be further transformed to:

$$\Delta E = \frac{e}{m_e^2 c^2} \boldsymbol{s} \cdot \left(\frac{\partial\phi}{\partial r} \frac{1}{r} \boldsymbol{r} \times \boldsymbol{p} \right) = \frac{e\hbar}{2 m_e^2 c^2} \frac{1}{r} \frac{\partial\phi}{\partial r} \boldsymbol{\sigma} \cdot \boldsymbol{L} \tag{2.18}$$

Thus $\Delta E \propto \boldsymbol{L} \cdot \boldsymbol{S}$, the expected result for the spin-orbit coupling. In the next section, we will see that the proportionality constant in equation (2.18) only differs from the relativistic result by a factor of 1/2. This factor comes from the lack of a full Lorentz transformation in this simple derivation [19]. However, it is still astonishing that this crude approximation yields such a good result.

---

[3] This has to be introduced ad-hoc in this semi-classical approach.

2.1.2.1 Relativistic origin

The following derivations follow mainly [19, 20, 21].

Relativistic Quantum Mechanics: As the spin-orbit coupling is a relativistic effect, we will first have to take a look at relativistic quantum mechanics.

As the Schroedinger equation $i\hbar\partial_t\psi = -\hbar^2/2m\ \nabla^2\psi$ is of different order in derivatives ∂_t and ∂_x it cannot be Lorentz invariant and thus cannot be a relativistic wave equation.

By looking at the dispersion relation from Einstein's special theory of relativity

$$E^2 = m^2c^4 + c^2p^2 \tag{2.19}$$

Paul Dirac postulated the *Dirac equation* (1928) as the relativistic counterpart to the Schroedinger equation:

$$i\hbar\frac{\partial}{\partial t}\psi = \left(-i\hbar c\ \alpha^k\partial_k + \beta mc^2\right)\psi = H\psi \tag{2.20}$$

It can be shown that α and β have to fulfill the following equations, for the Dirac equation to fulfill Lorentz invariance [19]:

$$\alpha^i\alpha^j + \alpha^j\alpha^i = 2\delta^{ij} \tag{2.21}$$

$$\alpha^i\beta + \beta\alpha^i = 0 \tag{2.22}$$

$$(\alpha^i)^2 = \beta^2 = \mathbb{1} \tag{2.23}$$

Thus, α^i and β are not numbers but $N \times N$ matrices (they have to anticommute) and the 'wave function' ψ from equation (2.20) is a N-sized column vector $\psi = (\psi_1 \dots \psi_N)^T$.

It can be further shown, that the smallest matrices fulfilling equation (2.21)-(2.23) are of size 4×4. They can be represented as:

$$\alpha^k = \begin{pmatrix} 0 & \sigma^k \\ \sigma^k & 0 \end{pmatrix}, \quad \beta = \begin{pmatrix} \mathbb{1}_{2\times2} & 0 \\ 0 & -\mathbb{1}_{2\times2} \end{pmatrix} \tag{2.24}$$

with $\mathbb{1}_{2\times2}$ being the 2×2 unity matrix and σ^k being the well-known Pauli matrices:

$$\sigma^1 = \begin{pmatrix} 0 & 1 \\ 1 & 0 \end{pmatrix}, \quad \sigma^2 = \begin{pmatrix} 0 & -i \\ i & 0 \end{pmatrix}, \quad \sigma^3 = \begin{pmatrix} 1 & 0 \\ 0 & -1 \end{pmatrix} \tag{2.25}$$

Introducing new Dirac matrices $\gamma^0 = \beta, \quad \gamma^i = \beta\alpha^i$, the Dirac equation can be further brought into its covariant form:

$$\left(-i\gamma^\mu\partial_\mu + \frac{mc}{\hbar}\right)\psi = 0 \tag{2.26}$$

Fouldy-Wouthuysen transformation: In the weakly relativistic limit, the 4-component spinor ψ can be decomposed into two parts

$$\psi = \begin{pmatrix} \varphi \\ \chi \end{pmatrix} \tag{2.27}$$

It can be shown that $\varphi/\chi \sim \mathcal{O}(c/v)$, thus φ is called the 'large component' and χ the 'small component' of ψ. Our goal is now to find a transformation that decouples the large and small component.

Without going too much into detail (the interested reader is best referred to [19]), this so-called Fouldy-Wouthuysen transformation together with a series expansion in $1/m$ leads to the following form of the Dirac equation for electrons (large components) in an electromagnetic field ($H = \boldsymbol{\alpha} \cdot (\boldsymbol{p} - e\boldsymbol{A}) + \beta m + e\phi$):

$$\begin{aligned} i\frac{\partial}{\partial t}\varphi = \Bigg\{ & m + e\phi + \frac{1}{2m}(\boldsymbol{p} - e\boldsymbol{A})^2 - \frac{e}{2m}\boldsymbol{\sigma} \cdot \boldsymbol{B} \\ & - \frac{\boldsymbol{p}^4}{8m^3} - \frac{e}{4m^2}\boldsymbol{\sigma} \cdot [\boldsymbol{E} \times (\boldsymbol{p} - e\boldsymbol{A})] - \frac{e}{8m^2}\nabla \cdot \boldsymbol{E} \Bigg\} \varphi \end{aligned} \tag{2.28}$$

The first line in equation (2.28) is exactly the Pauli equation[4], which is the result of the *non relativistic* expansion of the Dirac equation. The second line in (2.28) are three relativistic correction terms, namely the mass term, spin-orbit coupling and Darwin correction.

The spin-orbit term can be put into a more common form using the same method as in going from equation (2.17) to (2.18). The three correction terms then read:

$$H_1 = -\frac{(\boldsymbol{p}^2)^2}{8m^3} \qquad \text{...relativistic mass correction} \tag{2.29}$$

$$H_2 = \frac{e}{4m^2}\frac{1}{r}\frac{\partial \phi}{\partial r}\boldsymbol{\sigma} \cdot \boldsymbol{L} \qquad \text{...spin-orbit coupling} \tag{2.30}$$

$$H_3 = -\frac{e}{8m^2}\nabla^2 \phi(\boldsymbol{x}) \qquad \text{...Darwin term} \tag{2.31}$$

For Hydrogen-like atoms ($\phi \propto -Z/r$) it is obvious that $\frac{1}{r}\frac{\partial \phi}{\partial r} \propto Z/r^3$ and thus it can be shown that the spin-orbit coupling is especially important for heavier atoms (like Ir with $Z = 77$):

$$\langle H_2 \rangle \propto Z \left\langle 1/r^3 \right\rangle \propto Z^4/n^3 \tag{2.32}$$

---

[4] Plus the rest energy term $mc^2\varphi$ in natural units ($c = 1$).

2.1.2.2 SOC in t_{2g} orbitals

We now want to evaluate the $\boldsymbol{L} \cdot \boldsymbol{S}$ term in the $t_{2\mathrm{g}}$ subspace of the d-orbitals. As shown in section 2.1.1, we can use the T-P equivalence (2.15). Thus, starting from the $\boldsymbol{L}^{\mathrm{p,\,cub}}$ operators from equation (2.14) and introducing spin-operators $\boldsymbol{S} = \hbar\boldsymbol{\sigma}/2$ (with $\boldsymbol{\sigma}$ being the Pauli matrices) we get (again $\hbar = 1$, order of basis $p_{x\uparrow}, p_{y\uparrow}, p_{z\uparrow}, p_{x\downarrow}, p_{y\downarrow}, p_{z\downarrow},$):

$$\boldsymbol{L}^{\mathrm{p,cub}} \cdot \boldsymbol{S} = \frac{1}{2}\begin{bmatrix} 0 & 0 & 0 & 0 & 1 & 1 \\ 0 & 0 & 1 & 1 & 0 & 0 \\ 0 & 1 & 0 & -1 & 0 & 0 \\ 0 & 1 & -1 & 0 & 0 & 0 \\ 1 & 0 & 0 & 0 & 0 & -1 \\ 1 & 0 & 0 & 0 & -1 & 0 \end{bmatrix} \tag{2.33}$$

When considering the $t_{2\mathrm{g}}$ subspace, we must not forget the minus-sign from the TP-equivalence. However, this just changes all the signs in matrix (2.33). Diagonalizing the resulting matrix leads to the eigenvalues 1 (2-fold degenerate) and $-1/2$ (4-fold degenerate). The matrix of eigenvectors is

$$\begin{bmatrix} 0 & 1/\sqrt{3} & 0 & 1/\sqrt{6} & 0 & 1/\sqrt{2} \\ -1/\sqrt{3} & 0 & 2/\sqrt{6} & 0 & 0 & 0 \\ 1/\sqrt{3} & 0 & 1/\sqrt{6} & 0 & 1/\sqrt{2} & 0 \\ 1/\sqrt{3} & 0 & 1/\sqrt{6} & 0 & -1/\sqrt{2} & 0 \\ 0 & -1/\sqrt{3} & 0 & 2/\sqrt{6} & 0 & 0 \\ 0 & -1/\sqrt{3} & 0 & -1/\sqrt{6} & 0 & 1/\sqrt{2} \end{bmatrix} \tag{2.34}$$

This eigenbasis corresponds to the so-called *effective j-basis*, in which $\boldsymbol{J}^2$ and J^z are diagonal and thus good quantum numbers ($\boldsymbol{J} = \boldsymbol{L} + \boldsymbol{S}$). The same matrix can be calculated, when using the Clebsch-Gordan coefficients for $1 \times \frac{1}{2}$ ($l \times s$) together with our definition of the cubic harmonics for $l = 1$ (2.14).

It can also be seen in equation (2.34) that by rearranging the basis order, the matrix actually decomposes into a block-diagonal form consisting of two 3×3 blocks (with mixed spin). It can be shown that this decomposition into two blocks is also valid for the full d-shell [22]. This is used by TRIQS to decompose the Green's function into smaller blocks (see section 3.2.2.2).

2.1.2.3 LS and jj Coupling

For isolated atoms the Hund's rules describe the arrangement of spins and angular momenta in the ground state. Firstly, the total spin $S = \sum m_s$ is maximized, then the orbital angular momentum $L = \sum m_l$ is minimized. Thirdly, the total angular momentum J is chosen depending on the orbital's filling. For less than half-filling $J = |L - S|$, for more than half-filling $J = (L + S)$.

One has to take care when using this last rule in conjunction with TP-equivalence: As the third Hund's rule comes from minimizing spin-orbit coupling energies, the minus-sign in the TP-equivalence (2.15) flips the behaviour of this rule: For less than half-filled $t_{2\mathrm{g}}$ orbitals $J = (L + S)$, for more than half-filled $t_{2\mathrm{g}}$ orbitals $J = |L - S|$.

However, Hund's rules are only valid if $J_H \gg \lambda$. In this regime it is assumed that the spins of the single atoms $\boldsymbol{s}_i$ couple to a total spin $\boldsymbol{S} = \sum_i \boldsymbol{s}_i$ and the orbital angular momenta $\boldsymbol{l}_i$ to a total orbital angular momentum $\boldsymbol{L} = \sum_i \boldsymbol{l}_i$. These momenta then couple to a total angular momentum $\boldsymbol{J} = \boldsymbol{L} + \boldsymbol{S}$, which is why this regime is commonly called LS coupling.

For larger SOC λ the individual momenta $\boldsymbol{s}_i$ and $\boldsymbol{l}_i$ are no longer good quantum numbers, as the operators $\boldsymbol{S}$ and $\boldsymbol{L}$ no longer commute with the Hamiltonian. In this regime the individual electron's angular momenta $\boldsymbol{j}_i$ couple to a total angular momentum $\boldsymbol{J} = \sum_i j_i$, thus it is called jj coupling.

2.1.3 Ordered spin structures

2.1.3.1 Exchange Interaction

The ordering of spins in a system is a process driven by exchange interactions. To see what this means, we will first focus on a simple system, consisting of two electrons interacting with each other (neglecting spin-orbit coupling). The Hamiltonian can thus be written as

$$H = H_0(\boldsymbol{r}_1) + H_0(\boldsymbol{r}_2) + \frac{e^2}{|\boldsymbol{r}_1 - \boldsymbol{r}_2|} \tag{2.35}$$

Using Slater-determinants as an ansatz, we come to the well known result of a singlet state and a triply degenerate triplet state, with the corresponding energies E_s and E_t [23]:

$$E_s = E_1 + E_2 + K_{12} + J_{12} \tag{2.36}$$

$$E_t = E_1 + E_2 + K_{12} - J_{12} \tag{2.37}$$

with the density-density energy K_{12} and the exchange energy J_{12} defined as:

$$K_{12} = \int \mathrm{d}r_1 \, \mathrm{d}r_2 \frac{e^2}{r_{12}} |\varphi_1(\boldsymbol{r}_1)|^2 |\varphi_2(\boldsymbol{r}_2)|^2 \tag{2.38}$$

$$J_{12} = \int \mathrm{d}r_1 \, \mathrm{d}r_2 \varphi_1^*(\boldsymbol{r}_1)\varphi_2^*(\boldsymbol{r}_2) \frac{e^2}{r_{12}} \varphi_2(\boldsymbol{r}_1)\varphi_1(\boldsymbol{r}_2) \tag{2.39}$$

Dirac showed [24] that the same eigenvalue problem is obtained when considering just spins interacting with each other. This leads to a Hamiltionian of the form $H = \text{const} - \frac{1}{4}J\boldsymbol{\sigma}_1\boldsymbol{\sigma}_2$. Extending the approach above to multiple electrons on multiple atoms and introducing Wannier functions (to make the wavefunctions orthogonal again) leads to the well known Heisenberg model (an in-depth calculation can be found e.g. in [23]):

$$H = -\frac{1}{4}\sum_{i \neq j} J_{ij}\boldsymbol{\sigma}_i \cdot \boldsymbol{\sigma}_j \tag{2.40}$$

2.1.3.2 (Anti-) ferromagnetism of localized interacting moments

We are now looking at a system of localized moments driven by an external magnetic field. The external field can be split into Fourier components and we can look at the response to one single component:

$$\boldsymbol{H}(\boldsymbol{r}) = H\boldsymbol{e}_z \cos \boldsymbol{q}\boldsymbol{r} \tag{2.41}$$

With the Fourier transform of the Spin operators $\boldsymbol{S}_i$

$$\boldsymbol{S}(\boldsymbol{q}) = \int \mathrm{d}r e^{-i\boldsymbol{q}\boldsymbol{r}}\boldsymbol{S}(\boldsymbol{r}) = \sum_i e^{-i\boldsymbol{q}\boldsymbol{R}_i}\boldsymbol{S}_i \tag{2.42}$$

the total Hamiltonian can be written as a sum of the two contributions (2.40) and $\boldsymbol{H} \cdot \boldsymbol{S}$:

$$\begin{aligned} H &= -\sum_{i \neq j} J_{ij}\boldsymbol{S}_i\boldsymbol{S}_j + g\mu_B H \sum_i S_i^z \cos \boldsymbol{q}\boldsymbol{R}_i = \\ &= -\sum_{\boldsymbol{q}'} J(-\boldsymbol{q}')\boldsymbol{S}(\boldsymbol{q}')\boldsymbol{S}(-\boldsymbol{q}') + \frac{1}{2}g\mu_B H[S^z(\boldsymbol{q}) + S^z(-\boldsymbol{q})] \end{aligned} \tag{2.43}$$

with

$$J(-\boldsymbol{q}') = \frac{1}{N}\sum_{i \neq j} J_{ij}e^{-i\boldsymbol{q}'(\boldsymbol{R}_i - \boldsymbol{R}_j)} \tag{2.44}$$

Taking a mean-field approach in equation (2.43) is called Random-Phase approximation (RPA). After some calculations (the full derivation can be again found in [23]) it yields the system's susceptibility and critical temperature:

$$\chi_{\mathrm{RPA}}(\boldsymbol{q}) = \frac{C}{T - J(\boldsymbol{q})C\Omega/(g\mu_B)^2} \tag{2.45}$$

$$T_c = \frac{J(\boldsymbol{Q})C\Omega}{(g\mu_B)^2} \tag{2.46}$$

In equation (2.46) $\boldsymbol{Q}$ is the wave-vector which yields the maximal $J(\boldsymbol{q})$. As $J(\boldsymbol{q})$ contains information about the crystal structure (see equation (2.44)), different (anti-) ferromagnetic solutions are possible, depending on the problem at hand.

2.1.4 Green's functions

Here just a brief overview of the broad field of Green's functions relevant for this thesis is given. For the derivation of the listed properties of these functions, the interested reader is referred to literature (e.g. [25]).

We will limit ourselves to fermionic Green's functions as they will be applied to a system of electrons in the scope of this work.

Retarded Green's function: Green's functions are introduced in the context of linear response theory as the correlation function between two (for now arbitrary) operators. The Retarded Green's function (in real time) for a system of fermions is defined as:

$$G^r_{AB}(t) = \langle\langle A(t), B(0) \rangle\rangle_t := -i\Theta(t)\left\langle \{A(t), B(0)\} \right\rangle \tag{2.47}$$

Imaginary time: When considering expectation values of the form

$$C = \langle A(t)B(t') \rangle = \frac{1}{Z}\,\mathrm{Tr}\left\{e^{-\beta H} A(t)B(t')\right\} \tag{2.48}$$

one runs into the problem of $e^{-\beta H}$ being real, while the time evolution operator e^{-iHt} is complex, preventing them from being treated in the same manner. One tackles this problem by introducing the imaginary time $\tau = it$ with the corresponding Matsubara Green's function:

$$G_{AB}(\tau, \tau') = -\left\langle T_\tau (A(\tau) B^\dagger(\tau')) \right\rangle \tag{2.49}$$

This imaginary time Green's function (for $\tau' = 0$) is defined on the interval $-\beta \leq \tau < \beta$ and is antiperiodic (for fermions), meaning $G_{AB}(\tau + \beta) = -G_{AB}(\tau)$. Thus, a Fourier transformation can be performed, leading to a Green's function defined on the discrete Matsubara frequencies $\omega_n = (2n + 1)\pi/\beta$:

$$G_{AB}(i\omega_n) = \int_0^\beta e^{i\omega_n \tau} G_{AB}(\tau)\,\mathrm{d}\tau \tag{2.50}$$

It can be shown that $G_{AB}(i\omega_n)$ and the Fourier transform $G^r_{AB}(\omega)$ of $G^r_{AB}(t)$ (2.47) are in fact two special cases of a Green's function $\mathcal{G}_{AB}(z)$

defined in the complex plane:

$$\mathcal{G}_{AB}(z = i\omega_n) = G_{AB}(i\omega_n) \tag{2.51}$$

$$\mathcal{G}_{AB}(z = \omega + i0^+) = G^r_{AB}(\omega + i0^+) \tag{2.52}$$

It can be shown that $\mathcal{G}(z)$ is analytic in the upper half of the complex plane. Thus it is possible to analytically continue the function from values on the Matsubara axis down to the real axis (see section 4.1.3.5).

Hermitian Symmetry: In this paragraph, we will see an interesting symmetry property of Matsubara Green's functions. Starting with the definition of an imaginary-time Green's function (2.49) we can prove:

$$\begin{aligned}
G_{AB}(\tau) &= -\left\langle A(\tau)B^\dagger(0)\right\rangle = \\
&= -\operatorname{Tr}\left\{\rho\, e^{-\tau H} A e^{\tau H} B^\dagger\right\} = \\
&= -\operatorname{Tr}\left\{B e^{\tau H} A^\dagger e^{-\tau H} \rho\right\}^* = \\
&= -\operatorname{Tr}\left\{\rho\, e^{-\tau H} B e^{\tau H} A^\dagger\right\}^* = G^*_{BA}(\tau)
\end{aligned} \tag{2.53}$$

Now, to go over to imaginary frequencies we take the Fourier transform of $G_{AB}(\tau)$:

$$\begin{aligned}
G_{AB}(i\omega_n) &= \int \mathrm{d}\tau\ G_{AB}(\tau) e^{-i\omega_n \tau} = \\
&= \int \mathrm{d}\tau\ G^*_{BA}(\tau) e^{-i\omega_n \tau} = \\
&= \left[\int \mathrm{d}\tau\ G_{BA}(\tau) e^{i\omega_n \tau}\right]^* = G^*_{BA}(-i\omega_n)
\end{aligned} \tag{2.54}$$

2.2 Band structure calculations

2.2.1 DFT

As mentioned in the beginning of section 2.1, the electron-electron interaction term is still problematic in the Born-Oppenheimer Hamiltonian. As it couples every electron with every other electron, one would have to consider a many-particle wave function $\psi(\boldsymbol{r}_1, \boldsymbol{r}_2, \ldots \boldsymbol{r}_N)$, depending on the coordinates of every electron in the system. For most real materials, the number of electrons in the unit cell easily exceeds the critical $N_{\max} \approx \mathcal{O}(10)$ for which a many-particle approach can be handled [26].

2.2.1.1 Hohenberg-Kohn theorems

The Hohenberg-Kohn theorems [27] justify the use of the electron density $n(\boldsymbol{r})$ instead of the many-particle wave function $\psi(\boldsymbol{r}_1, \boldsymbol{r}_2, \ldots \boldsymbol{r}_N)$ when calculating ground state properties.

Electron density as base variable: The first Hohenberg-Kohn theorem states that in a system of electrons in an external potential $v(\boldsymbol{r})$, the ground-state electron density $n(\boldsymbol{r})$ uniquely identifies this potential (apart from an additive constant) [27]. As the system's Hamiltonian is dependent on $v(\boldsymbol{r})$, the electron density also defines the Hamiltonian and thus the ground state wave function.

Variational principle: The ground state energy of a system can be calculated from the Rayleigh-Ritz variational principle, with $\tilde{\Psi}$ being a trial wave-function with the corresponding density $\tilde{n}(\boldsymbol{r})$:

$$E = \min_{\tilde{\Psi}} \left\langle \tilde{\Psi} \middle| H \middle| \tilde{\Psi} \right\rangle \tag{2.55}$$

The second Hohenberg-Kohn theorem states, that the correct electron density $n(\boldsymbol{r})$ minimizes equation (2.56) and returns the ground state energy E_0 [27].

$$E[n(\boldsymbol{r})] = \int v(\boldsymbol{r}) n(\boldsymbol{r}) d\boldsymbol{r} + F[n(\boldsymbol{r})] \tag{2.56}$$

$F[n(\boldsymbol{r})]$ is an universal functional, independent on the number of particles and the external potential. It contains the kinetic energy of the electrons as well as the potential energy of the electron-electron interaction.

As the electron-electron repulsion through Coulomb interaction is known, it can be separated out of $F[n(\boldsymbol{r})]$ [27]:

$$F[n(\boldsymbol{r})] = \frac{1}{2} \iint \frac{n(\boldsymbol{r}) n(\boldsymbol{r}\,')}{|\boldsymbol{r} - \boldsymbol{r}\,'|} d\boldsymbol{r} d\boldsymbol{r}\,' + G[n(\boldsymbol{r})] \tag{2.57}$$

2.2.1.2 Kohn-Sham equations

In the Kohn-Sham equations one considers (in analogy to the Hartree equation) a set of non-interacting, independent particles in an effective 'Kohn-Sham' potential $V_{KS}(\boldsymbol{r})$ [28]. For those particles the - now non-interacting - Schroedinger equation reads as follows:

$$\left[-\frac{1}{2} \nabla^2 + V_{KS}(\boldsymbol{r}) \right] \varphi_j(\boldsymbol{r}) = \epsilon_j \varphi_j(\boldsymbol{r}) \tag{2.58}$$

As a constraint, the Kohn-Sham potential $V_{KS}(\boldsymbol{r})$ has to be chosen in a way that the ground state density resembles the ground state density of the interacting system:

$$n_{KS}(\boldsymbol{r}) = \sum_j |\varphi_j(\boldsymbol{r})|^2 \overset{!}{=} n(\boldsymbol{r}) \tag{2.59}$$

For these non-interacting Kohn-Sham particles the energy can be simply written as ($T_0[n_{KS}(\boldsymbol{r})]$ being the kinetic energy):

$$E_{KS}[n_{KS}(\boldsymbol{r})] = T_0[n_{KS}(\boldsymbol{r})] + \int V_{KS}(\boldsymbol{r})n_{KS}(\boldsymbol{r})d\boldsymbol{r} \tag{2.60}$$

Looking at interacting electrons, we can now formally rewrite equations (2.56) and (2.57) [28], leading to:

$$E[n(\boldsymbol{r})] = \int v(\boldsymbol{r})n(\boldsymbol{r})d\boldsymbol{r} + \frac{1}{2}\iint \frac{n(\boldsymbol{r})n(\boldsymbol{r}')}{|\boldsymbol{r}-\boldsymbol{r}'|}d\boldsymbol{r}d\boldsymbol{r}' + E_{xc}[n(\boldsymbol{r})] + T_0[n(\boldsymbol{r})] \tag{2.61}$$

In this equation, $T_0[n(\boldsymbol{r})]$ is again the kinetic energy of the non-interacting system and $E_{xc}[n(\boldsymbol{r})]$ the so-called Exchange-Correlation energy, in which we have put all unknown interaction terms of the system.

Comparing equations (2.60) and (2.61) under the constraint of equation (2.59), one finds the following form of the Kohn-Sham potential:

$$V_{KS}(\boldsymbol{r}) = v(\boldsymbol{r}) + V_H(\boldsymbol{r}) + V_{xc}(\boldsymbol{r}) \tag{2.62}$$

with V_H being the Hartree potential and V_{xc} the Exchange-Correlation potential:

$$V_{xc}(\boldsymbol{r}) = \left.\frac{\delta E_{xc}[n'(\boldsymbol{r})]}{\delta n'(\boldsymbol{r})}\right|_{n(\boldsymbol{r})} \tag{2.63}$$

As $n(\boldsymbol{r})$ is in turn dependent on V_{xc}, one has to solve the Kohn-Sham equations iteratively in a self-consistent manner. A simple overview of this DFT cycle is shown in Figure 2.3.

2.2.1.3 Exchange-Correlation potential

Until now, no approximation has been taken and DFT is an exact theory up to this point. However, we have done this by just taking all unknown terms and putting them inside $V_{xc}(\boldsymbol{r})$. The exact analytic form of $V_{xc}(\boldsymbol{r})$ (and thus E_{ex}) remains unknown and approximations have to be taken at this point to make DFT usable for actual calculations.

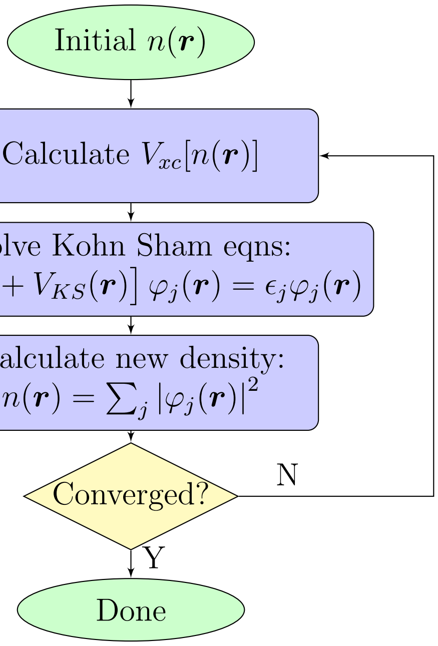
Initial $n(\boldsymbol{r})$
Calculate $V_{xc}[n(\boldsymbol{r})]$
Solve Kohn Sham eqns:
$\left[-\frac{1}{2}\nabla^2 + V_{KS}(\boldsymbol{r})\right]\varphi_j(\boldsymbol{r}) = \epsilon_j\varphi_j(\boldsymbol{r})$
Calculate new density:
$n(\boldsymbol{r}) = \sum_j |\varphi_j(\boldsymbol{r})|^2$
Converged?
N
Y
Done

Figure 2.3 – DFT loop

As the most important approximations in E_{xc} are quasi-local [26], we can look at it in the following form:

$$E_{xc}[n(\boldsymbol{r})] = \int e_{xc}(\boldsymbol{r}, [n(\tilde{\boldsymbol{r}})])n(\boldsymbol{r})d\boldsymbol{r} \tag{2.64}$$

In this general form, the energy density $e_{xc}(\boldsymbol{r}, [n(\tilde{\boldsymbol{r}})])$ at the point $\boldsymbol{r}$ depends on the electron density $n(\tilde{\boldsymbol{r}})$ in the whole space. However, in real systems e_{xc} primarily depends on the density $n(\tilde{\boldsymbol{r}})$ at points $\tilde{\boldsymbol{r}}$ near[5] $\boldsymbol{r}$.

Two classes of the most widespread Exchange-Correlation potentials are the Local-Density approximation (LDA), where the energy is only dependent on the density at the same point, and the GGA approximations (most famously the PBE potential [29]), where also the gradient of the density is taken into account.

$$E_{xc}^{LDA}[n(\boldsymbol{r})] = \int e_{xc}[n(\boldsymbol{r})]n(\boldsymbol{r})d\boldsymbol{r} \tag{2.65}$$

$$E_{xc}^{GGA}[n(\boldsymbol{r})] = \int e_{xc}[n(\boldsymbol{r}), \nabla n(\boldsymbol{r})]n(\boldsymbol{r})d\boldsymbol{r} \tag{2.66}$$

One common further approximation is to replace the energy functional $e_{xc}[n(r)]$ by the energy density of the homogeneous electron gas $e_{xc}^{\text{HEG}}(n)$

---

[5] 'Near' in the order of the Fermi wavelength or the Thomas-Fermi screening length [26].

which is not a functional anymore. Thus, the LDA-Exchange-Correlation energy can be written as:

$$E_{xc}^{LDA}[n(\boldsymbol{r})] = \int e_{xc}^{\mathrm{HEG}}(n)n(\boldsymbol{r})d\boldsymbol{r} \tag{2.67}$$

2.2.2 DMFT

While DFT gives good results in comparison with experiments for many applications in physics and chemistry, its (local) density-based approach fails for strongly localized electrons (such as *d*- and *f*-shell electrons of transition metals). For these strongly-correlated materials (see section 1.1), a different approach has to be taken to take into account interactions which lead to interesting many-body phenomena.

The dynamical mean-field theory (DMFT) [30] is one way to tackle this problem by mapping the interacting lattice problem to a single-site effective problem with less degrees of freedom [30]. Due to similarities with DMFT (both being self-consistent mean-field theories), let's first review the classical mean-field theroy of the well known Ising-model.

2.2.2.1 Classical mean-field

Using classical MF theory, we try to solve the Ising Hamiltonian:

$$H_{\mathrm{Ising}} = -\sum_{<ij>} J_{ij} S_i S_j - h \sum_i S_i \tag{2.68}$$

We map this (interacting) Hamiltonian onto a non-interacting auxiliary problem, with independent spins in an effective field h_{eff}:

$$H_{\mathrm{eff}} = -\sum_i h_i^{\mathrm{eff}} S_i \tag{2.69}$$

In this effective model, we can easily calculate the magnetization m_{MF} [31]:

$$m_{\mathrm{MF}} = \tanh\left(\beta h^{\mathrm{eff}}\right) \tag{2.70}$$

We need to chose h_{eff} in a way so that the desired expectation values (the magnetization in the case of the Ising model) in the effective model (2.70) reproduces the values of the original model ($m_i = \langle S_i \rangle$). To do so, we have to take an approximation by neglecting the fluctuation terms

$$(S_i - \langle S_i \rangle)(S_j - \langle S_j \rangle) = S_i S_j - S_i \langle S_j \rangle - S_j \langle S_i \rangle + \underbrace{\langle S_i \rangle \langle S_j \rangle}_{\text{neglectable}} \overset{!}{=} 0 \tag{2.71}$$

which, after some simple calculations, leads to the known self-consistency condition for ferromagnetic systems (z being the coordination number):

$$h_{\text{eff}} = Jzm - h \tag{2.72}$$

$$m_{\text{MF}} = \tanh\left(\beta h + z\beta Jm\right) \tag{2.73}$$

As m_{MF} is dependent on m, which in turn is approximated by m_{MF}, this equation can be solved iteratively[6]. The resulting mean-field loop is shown in Fig. 2.4 in a simplified manner. In actual calculations, such forward iterative methods can lead to instabilities, which can be improved by mixing the results from earlier iterations (damping).

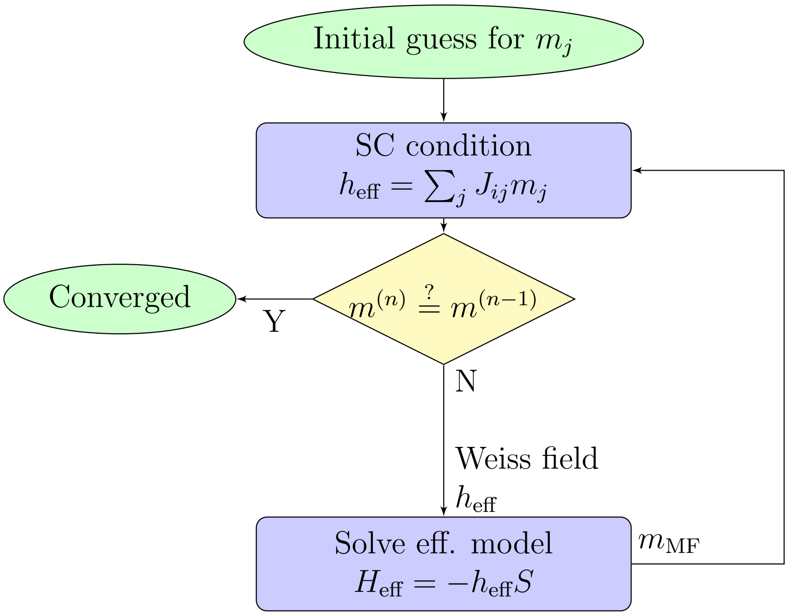
Initial guess for m_j
SC condition
$h_{\text{eff}} = \sum_j J_{ij} m_j$
$m^{(n)} \overset{?}{=} m^{(n-1)}$
Converged
Y
N
Weiss field
h_{eff}
Solve eff. model
$H_{\text{eff}} = -h_{\text{eff}} S$
m_{MF}

Figure 2.4 – Simplified mean field loop for the Ising model

2.2.2.2 DMFT basics

Lattice- and Impurity model: Following the derivation in [31], we will look at a single-band Hubbard model:

$$H = -\sum_{ij,\sigma} t_{ij} c^{\dagger}_{i\sigma} c_{j\sigma} + U \sum_{i} n_{i\uparrow} n_{i\downarrow} + \varepsilon_0 \sum_{i\sigma} n_{i\sigma} \tag{2.74}$$

---

[6] For the Ising model, equation (2.73) can be solved graphically. As this is not possible in general, it will not be discussed here in detail.

As mentioned above, we will map the lattice problem (2.74) onto an Anderson-Impurity model of a single site coupled to a bath (see Fig. 2.5). In the impurity model (2.75), new fermionic bath operators $a_{l\sigma}$ are introduced as additional degrees of freedom:

$$
\begin{aligned}
H_{AIM} &= H_{\text{atom}} + H_{\text{bath}} + H_{\text{coupling}} && (2.75)\\
H_{\text{atom}} &= U n^c_\uparrow n^c_\downarrow - \mu(n^c_\uparrow + n^c_\downarrow) && (2.76)\\
H_{\text{bath}} &= \sum_{l\sigma} \tilde{\varepsilon}_l a^\dagger_{l\sigma} a_{l\sigma} && (2.77)\\
H_{\text{coupling}} &= \sum_{l\sigma} V_l (a^\dagger_{l\sigma} c_\sigma + a_{l\sigma} c^\dagger_\sigma) && (2.78)
\end{aligned}
$$

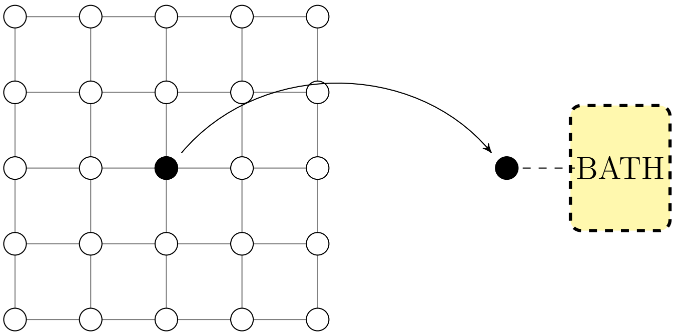

Figure 2.5 – Mapping of a lattice problem onto an impurity problem

Our goal now is to find the bath energies $\tilde{\varepsilon}_l$ and the hopping amplitudes V_l of the AIM (2.75) in a way so that the impurity's Green's function G_{imp} resembles the local lattice Green's function G_{loc}:

$$G_{\text{imp}} \overset{!}{=} G_{\text{loc}} = G_{ii,\text{lat}} \qquad (2.79)$$

Lattice and Impurity Green's functions: Using an action-based formalism ($Z = \int \mathcal{D}c^\dagger \mathcal{D}c e^S$), the effective action S_{eff} of the AIM (bath degrees of freedom integrated out) can be written as [31]:

$$S_{\text{eff}} = -\int_0^\beta \mathrm{d}\tau \int_0^\beta \mathrm{d}\tau' \sum_\sigma c^\dagger_\sigma(\tau) G^{-1}_{0,\text{imp}}(\tau-\tau') c_\sigma(\tau') + U \int_0^\beta \mathrm{d}\tau n_\uparrow(\tau) n_\downarrow(\tau) \qquad (2.80)$$

With $G_{0,\text{imp}}$ being the Weiss field of DMFT, defined as

$$G_{0,\text{imp}}(i\omega_n) = [i\omega_n + \mu - \varepsilon_0 - \Delta(i\omega_n)]^{-1} \qquad (2.81)$$

and the hybridisation function $\Delta(i\omega_n)$ containing the AIM parameters from equation (2.75):

$$\Delta(i\omega_n) = \sum_l \frac{|V_l|^2}{i\omega_n - \tilde{\varepsilon}_l} \tag{2.82}$$

For the lattice Green's function, one starts from the usual definition of an interacting Green's function with the self-energy $\Sigma(\boldsymbol{k}, i\omega_n)$:

$$G_{\text{lat}}(\boldsymbol{k}, i\omega_n) = [i\omega_n + \mu - \varepsilon_{\boldsymbol{k}} - \Sigma(\boldsymbol{k}, i\omega_n)]^{-1} \tag{2.83}$$

2.2.2.3 DMFT loop

DMFT, as its name suggests, is a mean-field theory (the 'dynamic' meaning that the Weiss feld is a function of frequency). Looking at the analogies between MF theroy and DMFT, it is obvious that our effective model will be the AIM (2.75). The Weiss field is, as mentioned above, the non-interacting impurity Green's function $G_{0,\text{imp}}$ from equation (2.81).

Solving the AIM (for details on how to do that see section 2.2.2.5) with a given $G_{0,\text{imp}}$ gives us the interacting impurity Green's function G_{imp} as well as the impurity self-energy Σ_{imp} (connected via the Dyson equation $G = [G_0^{-1} - \Sigma]^{-1}$). We now approximate the lattice self-energy Σ_{lat} by the impurity self-energy:

$$\Sigma_{\text{lat}}(k, i\omega_n) \equiv \Sigma_{\text{lat}}(i\omega_n) \approx \Sigma_{\text{imp}}(i\omega_n) \tag{2.84}$$

Taking the definition of an interacting Green's function (2.83), we can write the local part of the lattice Green's function in terms of Σ_{imp}:

$$G_{\text{loc}}(i\omega_n) := G_{ii,\text{lat}}(i\omega_n) = \sum_k \frac{1}{i\omega_n + \mu - \varepsilon_k - \Sigma_{\text{imp}}} \overset{!}{=} G_{\text{imp}}(i\omega_n) \tag{2.85}$$

In this equation, the $\overset{!}{=}$ on the right side is again our MF self-consistency condition (2.79). This will become more obvious when we insert the definition of the Weiss field (2.81) into (2.85):

$$\sum_k \frac{1}{\Delta(i\omega_n) + G_{\text{imp}}^{-1}(i\omega_n) - \varepsilon_k} = G_{\text{imp}}(i\omega_n) \tag{2.86}$$

In analogy to equation (2.73) from classical mean-field we now have an expression where we 'just' have to find the right $\Delta(i\omega_n)$ that fulfills the equation for our given ε_k from the original model. Again, this is done self-consistenty, the resulting DMFT loop can be found in Fig. 2.6. Furthermore, Tab. 2.1 summarizes the similarities between MFT and DMFT outlined in this paragraph.

Table 2.1 – Comparison between DMFT for the Hubbard model and MFT for the Ising model (taken and modified from [31]), as well as comparison with Kohn-Sham density functional theory (DFT) [32].

	DMFT		MFT Ising		DFT	
Hamiltonian	$H_{\text{Hubbard}} = -\sum_{ij,\sigma} t_{ij} c_{i\sigma}^{\dagger} c_{j\sigma} + H_{\text{atom}}$ (interacting)	(2.74)	$H_{\text{Ising}} = -\sum_{<ij>} J_{ij} S_i S_j$ (interacting)	(2.68)	H_{BO} (interacting)	(2.2)
Local observable	$G_{ii}(i\omega_n) = \left\langle\left\langle c_{i\sigma}; c_{i\sigma}^{\dagger} \right\rangle\right\rangle$		$m_i = \langle S_i \rangle$		$n(\boldsymbol{r}) = \sum_i \lvert\psi_i(\boldsymbol{r})\rvert^2$	
Effective model	$H_{\text{AIM}} = H_{\text{atom}} + H_{\text{bath}} + H_{\text{coupling}}$ (interacting)	(2.75)	$H_{\text{eff}} = -h_{\text{eff}} S$ (non-interacting)	(2.69)	H_{KS} (non-interacting)	(2.58)
Weiss field	$G_{0,\text{imp}}(i\omega_n)$ (dynamic)	(2.81)	h_{eff} (static)	(2.72)	$V_{\text{KS}}(\boldsymbol{r})$ (static)	(2.62)
SC relation	$\sum_k [\Delta(i\omega_n) + G_{\text{imp}}^{-1}(i\omega_n) - \varepsilon_k]^{-1} = G_{\text{imp}}(i\omega_n)$	(2.86)	$h_{\text{eff}} = \sum_j J_{ij} m_j$	(2.73)	$n_{KS}(\boldsymbol{r}) = n(\boldsymbol{r})$	(2.59)

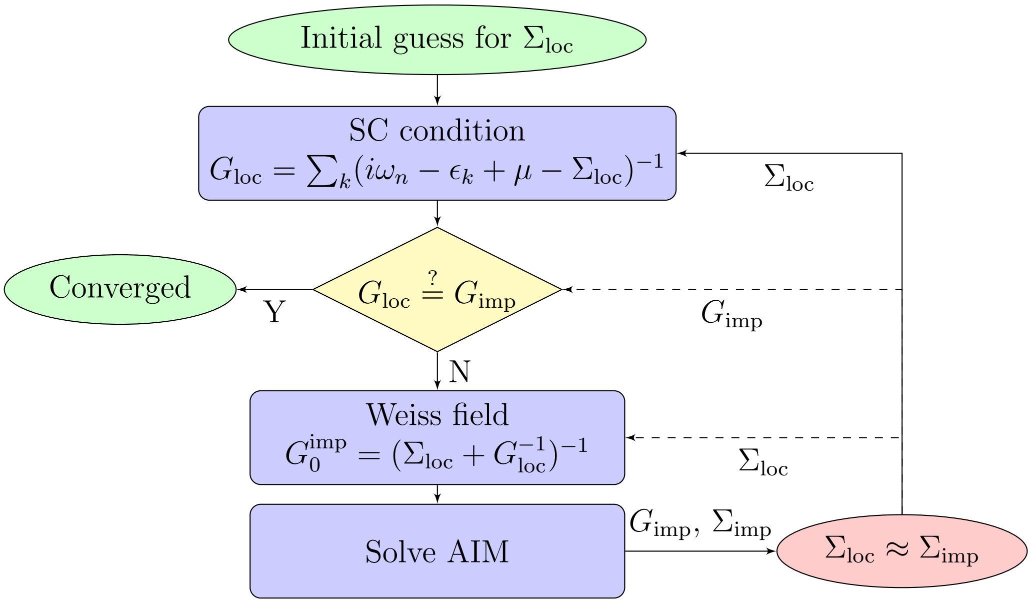
Initial guess for Σ_{loc}
SC condition
$G_{\text{loc}} = \sum_k (i\omega_n - \epsilon_k + \mu - \Sigma_{\text{loc}})^{-1}$
Σ_{loc}
Converged
Y
$G_{\text{loc}} \overset{?}{=} G_{\text{imp}}$
G_{imp}
N
Weiss field
$G_0^{\text{imp}} = (\Sigma_{\text{loc}} + G_{\text{loc}}^{-1})^{-1}$
Σ_{loc}
Solve AIM
G_{imp}, Σ_{imp}
$\Sigma_{\text{loc}} \approx \Sigma_{\text{imp}}$

Figure 2.6 – DMFT loop

2.2.2.4 Exact limits of DMFT

DMFT becomes exact in three limits. As the atomic limit ($t_{ij} = 0$) and the non-interacting limit ($U = 0$) lie on the two different ends of possible parameters, DMFT can be seen as an interpolation for the parameters in between.

Non-interacting limit: In the non-interacting limit $U = 0$, the self-energy becomes zero:

$$\Sigma(i\omega_n) = 0 \tag{2.87}$$
$$\rightarrow G_{0,\text{imp}}(i\omega_n) = G_{\text{imp}}(i\omega_n) \tag{2.88}$$

and equation (2.85) becomes trivial:

$$G_{\text{loc}}(i\omega_n) = \sum_k \frac{1}{i\omega_n + \mu - \varepsilon_k} \tag{2.89}$$

Atomic limit: In the atomic limit $t_{ij} = 0$ we are considering a model of isolated atoms. Thus $\varepsilon_k = 0$ (no k-dependence) and $\Sigma_{ij}(i\omega_n) = 0 \quad (i \neq j)$ becomes local.

With $\varepsilon_k = 0$ it can be seen from equation (2.86) that in that case the hybridization also becomes zero $\Delta(i\omega_n) = 0$. Thus the bath completely decouples from the system (isolated atom) and the DMFT-approximation becomes exact [31].

Infinite coordination: In the limit of infinite coordination number $z \to \infty$ DMFT, like classical mean field theory, becomes exact and the self-energy $\Sigma(i\omega_n)$ becomes local. This is not trivial to show, the reader is best referred to [31] and [33].

2.2.2.5 Impurity solvers

Now the question that remains is how to actually solve the impurity model. Unfortunately, no analytical solution is known for the AIM, so one has to rely on numerical methods. While methods such as iterative pertubation theory (ITP), exact diagonalization and renomalization group methods do exist, today's state-of-the-art methods are in general quantum Monte-Carlo algorithms [34].

Algorithms such as Hirsch-Fye [35] use a discretization of the (imaginary) time interval into small slices $\Delta\tau$ (Suzuki-Trotter decomposition) and then applying a Hubbard-Stratonivich transformation to each slice [34, 35]. The problem when considering (strongly) interacting systems and measuring their Green's functions lies within this discretization. As the Green's function rapidly goes to zero, as τ increases, discretization errors may become large [34].

Continuous time quantum Monte-Carlo algorithms: CT-QMC methods use a partition function that does not need time discretization. Thus any discretization errors can be avoided. To do so, one starts by splitting up the Hamiltonian into two parts $H = H_a + H_b$. One then writes the partition function with respect to H_a and expands it in terms of H_b [34]:

$$\begin{aligned} Z &= \mathrm{Tr}\left[T_\tau e^{-\beta H_a} \exp\left\{-\int_0^\beta \mathrm{d}\tau H_b(\tau)\right\}\right] = \\ &= \sum_k (-1)^k \int_0^\beta \mathrm{d}\tau_1 \cdots \int_{\tau_{k-1}}^\beta \mathrm{d}\tau_k \,\mathrm{Tr}\left[e^{-\beta H_a} H_b(\tau_k) H_b(\tau_{k-1}) \dots H_b(\tau_1)\right] \end{aligned} \tag{2.90}$$

As the splitting in H_a and H_b is arbitrary, different expansions are possible (and implemented in various codes). For the scope of this work, a hybridization-expansion based solver was used (the actual solver will be introduced in more detail in section 3.1.3.2). This means $H_b = H_{\mathrm{Hyb}}$ ($\equiv H_{\mathrm{coupling}}$ from eqn. (2.75)), meaning the expansion from equation (2.90) is taken in the hybridization. This leads to the following expression for the partition function, which will be sampled using QMC [36]:

$$Z = \sum_k \int \prod_{i=1}^{k} \mathrm{d}\tau_i \, \mathrm{d}\tau_{i'} \sum_{\alpha_j \alpha_{j'}} w(k, \{\alpha_j, \alpha'_j, \tau_j, \tau'_j\}) \tag{2.91}$$

With Monte-Carlo weights $w(k, \{\alpha_j, \alpha'_j, \tau_j, \tau'_j\})$ defined as

$$\begin{aligned} &w(k, \{\alpha_j, \alpha'_j, \tau_j, \tau'_j\}) = \\ &\qquad \det_{1 \le i,j \le k} [\Delta_{\alpha_i, \alpha'_j}(\tau_i - \tau'_j)] * \mathrm{Tr}\left[\mathcal{T} e^{-\beta H_{\mathrm{loc}}} \prod_{i=1}^{k} c^{\dagger}_{\alpha_i}(\tau_i) c_{\alpha'_i}(\tau'_i) \right] \end{aligned} \tag{2.92}$$

Sign problem: As with all fermionic QMC calculation, the sign problem can be a limiting factor. To see where this sign problem comes from, we will follow the derivation from [37]. We start by looking at the expectation value of an arbitrary physical observable O:

$$\langle O \rangle = \frac{\sum_x O(x)\rho(x)}{\sum_x \rho(x)} \tag{2.93}$$

If $\rho(x)$ is positive definite, it can be associated with a probability and the r.h.s. of equation (2.93) can be Monte-Carlo sampled [37]. However in fermionic systems negative signs can appear due to the Pauli principle (when two fermions are exchanged the configuration picks up a negative sign [38]).

One usually tackles this problem by splitting up $\rho(x)$ into its absolute value and a sign function $S(x) = \mathrm{sign}\ \rho(x)$, allowing Monte-Carlo sampling in the now positive definite distribution $|\rho(x)|$ (expectation values in this distribution are marked with a prime):

$$\langle O \rangle = \frac{\sum_x O(x)|\rho(x)|S(x)}{\sum_x |\rho(x)|S(x)} * \frac{\sum_x |\rho(x)|}{\sum_x |\rho(x)|} = \frac{\langle OS \rangle'}{\langle S \rangle'} \tag{2.94}$$

However, if $\langle S \rangle'$ becomes too small, small (statistical) fluctuations in $\langle S \rangle'$ can lead to large fluctuations in $\langle O \rangle$, rendering exact calculations impossible [37]. It can further be shown [38, 39] that the average sign goes like $\langle S \rangle' = \exp\{-\beta V \Delta f\}$, meaning the average sign quickly goes to zero for increasing problem size (V) and smaller temperature ($1/\beta$). This poses a limit for the applicability of QMC algorithms and is a yet unsolved problem.

2.2.3 DFT+DMFT

Our goal now is to combine well-established DFT calculations with DMFT for the interactions introduced by (for example) the Hubbard U-term. The motivation behind this DFT+DMFT approach is, as mentioned in the introduction and in section 2.2.1, that for transition metals and other strongly correlated materials DFT does not correctly describe the Mott-Insulator transition.

Note that in literature this approach is often also called 'LDA+DMFT', however that does not mean it is strictly limited to LDA-based exchange-correlation potentials and can also be used with GGA potentials.

2.2.3.1 From Bloch states to Wannier states

From our DFT calculation, we get the Kohn-Sham energies and wave-functions (see also equation (2.58), here $\boldsymbol{k}$ is the wave-vector in the first Brillouin-zone, σ the spin, ν the band index):

$$H_{\mathrm{KS}} \left|\varphi^{\sigma}_{\boldsymbol{k}\nu}\right\rangle = \varepsilon^{\sigma}_{\boldsymbol{k}\nu} \left|\varphi^{\sigma}_{\boldsymbol{k}\nu}\right\rangle \tag{2.95}$$

The basis spanned by all the $\left|\varphi^{\sigma}_{\boldsymbol{k}\nu}\right\rangle$ is referred to as the Bloch basis. In this basis we have delocalized electron bands and the basis spans the whole Hilbert space. The exact form of the basis functions is dependent on the used DFT code package. For details on the LAPW basis from Wien2k and its projection with dmftproj see sections 3.1.1 and 3.1.2 respectively.

Regardless of the used Bloch basis, for DMFT calculations we need to go over to a basis of *localized* Wannier-orbitals $\left|\chi^{\alpha\sigma}_{lm}\right\rangle$, with α being the atom index, σ the spin and (l, m) the orbital indices. As the l quantum-number is a static parameter of the problem at hand (for d-orbitals $l = 2$), it will be ommited in the orbitals' names. These Wannier-orbitals $\left|\chi^{\alpha\sigma}_{m}\right\rangle$ span the correlated subspace $\mathcal{C}$ of the Hilbert space. We can formally define a projection operator $P^{\mathcal{C}}_{\alpha}$ onto this subspace [40]:

$$P^{\mathcal{C}}_{\alpha} = \sum_{\left|\chi^{\alpha\sigma}_{m}\right\rangle \in \mathcal{C}} \left|\chi^{\alpha\sigma}_{m}\right\rangle \left\langle\chi^{\alpha\sigma}_{m}\right| \tag{2.96}$$

However, as $\mathcal{C}$ is just a subspace of the full Hilbert space, the sum in equation (2.96) is truncated at a certain point. One thus has to orthonormalize the resulting projectors.

2.2.3.2 Projection of the Green's function

In the Bloch basis we can write down the Green's function as ($\varepsilon^{\sigma}_{\boldsymbol{k}\nu}$ being the Kohn-Sham energies from equation (2.95)):

$$G^{\sigma}_{\nu\nu'}(\boldsymbol{k}, i\omega_n) = [(i\omega_n + \mu - \varepsilon^{\sigma}_{\boldsymbol{k}\nu})\delta_{\nu\nu'} - \Sigma^{\sigma}_{\nu\nu'}(\boldsymbol{k}, i\omega_n)]^{-1} \tag{2.97}$$

Coming from the (non-interacting) DFT calculation, $\Sigma^{\sigma}_{\nu\nu'}(\boldsymbol{k}, i\omega_n)$ is of course zero in the first step. To obtain the local Green's function we employ the projection defined in equation (2.96) and sum over the whole Brillouin zone [41]:

$$G^{\alpha\sigma}_{\text{loc},mm'}(i\omega_n) = \sum_{\boldsymbol{k},\nu\nu'} P^{\alpha\sigma}_{m,\nu}(\boldsymbol{k}) G^{\sigma}_{\nu\nu'}(\boldsymbol{k}, i\omega_n) [P^{\alpha\sigma}_{m,\nu}(\boldsymbol{k})]^{*} \tag{2.98}$$

with $P^{\alpha\sigma}_{m,\nu}(\boldsymbol{k})$ being the matrix elements of the projectors from equation (2.96) when multiplied with the Bloch basis-functions:

$$P^{\alpha\sigma}_{m,\nu}(\boldsymbol{k}) = \langle \chi^{\alpha\sigma}_{m} | \varphi^{\sigma}_{\boldsymbol{k}\nu} \rangle \tag{2.99}$$

With equation (2.98) we have a way to calculate the local Green's function from our DFT calculation. This will be the starting point of our DMFT calculation. However, to close the DMFT loop, we will have to introduce the AIM self energy back into equation (2.97).

2.2.3.3 Self energy and double counting

The process of transforming the impurity self-energy $\Sigma^{\alpha\sigma}_{\text{imp},mm'}(i\omega_n)$ back into Bloch-basis $\Sigma^{\sigma}_{\nu\nu'}(\boldsymbol{k}, i\omega_n)$ is called upfolding. Using the projectors from equation (2.98) in the 'other direction' yields:

$$\Sigma^{\sigma}_{\nu\nu'}(\boldsymbol{k}, i\omega_n) = \sum_{\alpha,mm'} [P^{\alpha\sigma}_{m,\nu}(\boldsymbol{k})]^{*} \Sigma'^{\alpha\sigma}_{mm'}(i\omega_n) P^{\alpha\sigma}_{m,\nu}(\boldsymbol{k}) \tag{2.100}$$

With $\Sigma'^{\alpha\sigma}_{mm'}(i\omega_n)$ being the double-counting corrected self-energy:

$$\Sigma'^{\alpha\sigma}_{mm'}(i\omega_n) = \Sigma^{\alpha\sigma}_{\text{imp},mm'}(i\omega_n) - \Sigma_{\text{DC},mm'} \tag{2.101}$$

This correction has to be taken, as some interaction effects are already accounted for in DFT (in form of the exchange-correlation potential) [42]. However, there is no analytic solution of how to exactly calculate this double-counting correction, but there are different approaches how to approximate it - three of which are implemented in the TRIQS/dfttools [43] package and shall be introduced briefly here:

Fully localized limit (FLL): The fully localized limit method [44] is based on the idea that LDA yields correct results for integer occupation numbers of orbitals ($n_{m\sigma} = 0$ or 1) [45]. This leads to the following formula for the double-counting self-energy:

$$[\Sigma_{\mathrm{FLL}}]^{\sigma}_{mm'} = \delta_{mm'} \left[U \cdot (N_{\mathrm{imp}} - \frac{1}{2}) - J \cdot (N^{\sigma}_{\mathrm{imp}} - \frac{1}{2}) \right] \tag{2.102}$$

with U and J being the Coulomb interaction and Hund's coupling, and $N^{(\sigma)}_{\mathrm{imp}}$ the (spin-resolved) average occupancy of the correlated site (impurity).

Around mean field (AMF): The around mean field method [46] is based on the opposite idea: correlation effects are accounted for in LDA, but only in an orbitally averaged manner [45]. The corresponding self-energy can be written (using $\widetilde{N^{\sigma}_{\mathrm{imp}}} = N^{\sigma}_{\mathrm{imp}}/\#_{\mathrm{dim}}$) as:

$$[\Sigma_{\mathrm{AMF}}]^{\sigma}_{mm'} = \delta_{mm'} \left[U \cdot (N_{\mathrm{imp}} - \widetilde{N^{\sigma}_{\mathrm{imp}}}) - J \cdot (N^{\sigma}_{\mathrm{imp}} - \widetilde{N^{\sigma}_{\mathrm{imp}}}) \right] \tag{2.103}$$

Held's formula: Held's convention [47] is implemented in TRIQS/dfttools as a mean-field formula for Kanamori-Hamiltonians [43]. It can be written as [40]:

$$[\Sigma_{\mathrm{Held}}]^{\sigma}_{mm'} = \delta_{mm'} (U - 2J)(N_{\mathrm{imp}} - 1) \tag{2.104}$$

Chapter 3

Implementation Details

3.1 Used code packages

Here the various code packages used in this work are briefly introduced. The calculations were run partly on computers of the Institute of Theoretical and Computational Physics (ITP) at the TU Graz and partly on the Vienna Scientific Cluster (VSC).

3.1.1 Wien2k

The DFT calculations were performed using Wien2k [48]. It features a fully linearized augmented plane wave (LAPW) basis set, splitting up the space into so called muffin-tin spheres S_{MT}^{α} around the atoms (atomic indices α, the radii of the spheres are set during the initialization) and a remaining interstitial region I.

Inside the muffin-tin spheres, the wave functions are expanded in radial functions times spherical harmonics around the nucleus, in the interstitial region plane waves are used. This means in the simplest case the basis can be written as (omitting spin indices):

$$\phi_{\boldsymbol{k}_n}(\boldsymbol{r}) = \begin{cases} \frac{1}{\sqrt{\omega}} e^{i\boldsymbol{k}_n \boldsymbol{r}} & \boldsymbol{r} \in I \\ \sum_{l,m} \left[A_{lm} u_l(\boldsymbol{r}, E_l) + B_{lm} \dot{u}(\boldsymbol{r}, E_l) \right] Y_{lm}(\hat{\boldsymbol{r}^{\alpha}}) & \boldsymbol{r} \in S_{\mathrm{MT}}^{\alpha} \end{cases} \tag{3.1}$$

In this equation, the $u(\boldsymbol{r}, E)$ are the solutions for the radial Schroedinger equation for the energy E. Other possible basis sets are added local orbitals (LO) for semicore bands, or APW(+lo). Regardless of the choice of basis, the wave functions can always be expressed as (now with spin explicit) [41]:

$$\psi^{\sigma}_{\boldsymbol{k},\nu}(\boldsymbol{r}) = \begin{cases} \frac{1}{\sqrt{\omega}} \sum_{|\boldsymbol{K}|\leq K_{\max}} c^{\sigma}_{\boldsymbol{K}\nu}(\boldsymbol{k}) e^{i(\boldsymbol{k}+\boldsymbol{K})\boldsymbol{r}} & \boldsymbol{r} \in I \\ \sum_{lm} [A^{\nu\alpha}_{lm} u^{\alpha\sigma}_{l}(r^{\alpha}, E^{\alpha}_{1l}) + B^{\nu\alpha}_{lm} \dot{u}^{\alpha\sigma}_{l}(r^{\alpha}, E^{\alpha}_{1l}) + & \\ \qquad + C^{\nu\alpha}_{lm} u^{\alpha\sigma}_{l}(r^{\alpha}, E^{\alpha}_{2l})] Y_{lm}(\hat{\boldsymbol{r}^{\alpha}}) & \boldsymbol{r} \in S^{\alpha}_{\mathrm{MT}} \end{cases} \tag{3.2}$$

3.1.1.1 SOC in Wien2k

Wien2k includes the relativistic terms differently for core and valence states. For the (fully occupied) core states a full relativistic treatment is possible. The valence states are first calculated in the *scalar relativistic approximation*, meaning that the SOC is ignored - making l and s good quantum numbers.

The spin-orbit coupling is then introduced using *second variational treatment*. For valence electrons inside the muffin-tin spheres, this means [49]:

$$H_1 \left|\psi\right\rangle = \varepsilon \left|\psi\right\rangle \qquad \text{(lapw1)} \tag{3.3}$$

$$(H_1 + H_{\mathrm{so}}) \left|\Psi\right\rangle = \epsilon \left|\Psi\right\rangle \qquad \text{(lapwso)} \tag{3.4}$$

Where the second equation is then expanded in the eigenbasis of the first equation (spin implicitly in the index i):

$$\sum_{i}^{N} \left(\delta_{ij}\varepsilon_j + \left\langle\psi_j\middle|H_{\mathrm{so}}\middle|\psi_i\right\rangle\right) \left\langle\psi_i\middle|\Psi\right\rangle = \epsilon \left\langle\psi_j\middle|\Psi\right\rangle \tag{3.5}$$

The number N is usually much smaller than the size of the original basis size, resulting in a smaller eigenvalue problem for H_{so} [50].

3.1.2 dmftproj

The projection onto the localized Wannier orbitals is done using dmftproj [41]. Its core functionality was already introduced in section 2.2.3.

For the calculations in the scope of this work, the `cubic` basis option was chosen. Furthermore it was necessary to perform the DFT calculation spin-polarized, as dmftproj does not support spin-orbit coupled calculations without spin-polarization (the calculation was performed spin-polarized but with fixed zero magnetic moment - all polarization effects are the accounted for in DMFT).

3.1.3 TRIQS

The DMFT calculations as well as the analysis were performed in TRIQS (Toolbox for research on interacting quantum systems) [51].

TRIQS offers an easy way to manipulate and store matrix-valued Green's functions and put them together into block Green's functions for block-diagonal problems. It also offers methods for second quantization operators, Hamiltonians and Monte-Carlo calculations.

For an in-depth introduction to TRIQS, one is best referred to its documentation [1], in section 3.2 an overview of the necessary functionalities used in this work is presented.

3.1.3.1 DFTTools

The DFTTools package [43] offers functionality for DFT-based material calculations in TRIQS. It allows to generate Green's functions out of the DFT data projected by dmftproj by performing the k-sum from equation (2.98) and has methods implemented to deal with double counting corrections and the upfolded self energy (see section 2.2.3.3).

3.1.3.2 CTHYB Solver

To solve the impurity model in the DMFT loop, a continous time hybridisation-expansion Monte-Carlo solver (CTHYB) [36] is used. Apart from doing the Monte-Carlo calculation in the hybridisation expansion, the CTHYB solver also tries to partition the Hilbert space by finding symmetries, thus minimizing the size of the matrices being multiplied [36].

3.1.3.3 MaxEnt

For the analytic continuation of the imaginary-frequency Green's function down to the real axis (see section 4.1.3.5), a MaxEnt-based algorithm [52] was used. As no off-diagonal elements had to be considered, the TauMaxEnt class from [52] could be used.

---

[1] `https://triqs.github.io/triqs/2.1.x/reference.html`, Accessed 26.2.2019

3.2 DMFT in TRIQS

In this section a brief overview of the computational tools used during this work is given, focusing on the technical aspects and problems one might encounter when running similar calculations.

All calculations below were performed using TRIQS version 1.4 [51] and dfttools version 1.4 [43].

3.2.1 From dmftproj to TRIQS

After generating the `almblm` files in Wien2k (x lapw2 −alm) dmftproj is called to generate the `ctqmcout`, `symqmc`, `parproj`, `sympar` and `oubwin` files. From these files, the HDF-archive is generated, using[2]:

```
import pytriqs.applications.dft.converters.wien2k_converter as
    ↪ wico

conv = wico.Wien2kConverter(filename = filename,hdf_filename=
    ↪ hdf_filename)
conv.convert_dft_input()
```

Listing 3.1 – Generation of HDF archive

Now all the information needed for the DMFT calculation is stored in this one HDF-file. One way to check whether the projection was successful is to plot the DOS in the Wannier basis. This is best done in a separate subdirectory (as it generates lots of files) and is done by:

```
from pytriqs.applications.dft import SumkDFTTools

SK = SumkDFTTools('MY_HDF_ARCHIVE.h5')

# mesh in eV
# broadening (additional Lorenz broadening), approx. 2*
    ↪ deltaOmega
SK.dos_wannier_basis(mesh=(-2,5,200), broadening=0.07,
    ↪ with_Sigma = False, with_dc = False)
```

Listing 3.2 – Calculating the DOS in Wannier basis

The resulting `dos_wann_ud_projX_Y_Z.dat` files (`X` being the number of correlated shell, `Y,Z` the orbital indices) can then be plotted to show the DOS[3].

---

[2] Also there exists a Python-script from Gernot Kraberger named w2kconv, capable of doing this plus other things (e.g. conversion for band calculations).

[3] This is best done using the plot_cid_grid script, which gives images like Fig. 4.4.

3.2.2 Basis transformations

As there are different ways to define basis transformations and the corresponding transformation matrices (for example where they are daggered), this paragraph introduces the conventions used in this thesis.

We define a unitary transformation matrix $T_{\mathcal{A}\to\mathcal{B}}$ (which we, for now, will just call T for simplicity) going from basis $\mathcal{A}$ to basis $\mathcal{B}$ such that a Green's function transforms like [4]

$$G^{\mathcal{B}} = TG^{\mathcal{A}}T^{\dagger} \tag{3.6}$$

For second quantization creation and anihilation operators ($a \in \mathcal{A}$ and $b \in \mathcal{B}$) this means:

$$\begin{aligned} b_i &= \sum\nolimits_j T_{ij} a_j & \qquad a_i &= \sum\nolimits_j T^*_{ji} b_j \\ b_i^{\dagger} &= \sum\nolimits_j T^*_{ij} a_j^{\dagger} & \qquad a_i^{\dagger} &= \sum\nolimits_j T_{ji} b_j^{\dagger} \end{aligned}$$

For the transformation of a two-particle operator (such as the interaction part of the Hamiltonian) one starts from the definition:

$$\hat{O} = \sum_{ijkl} U^{\mathcal{A}}_{ijkl} a_i^{\dagger} a_j^{\dagger} a_l a_k \tag{3.7}$$

Transforming to the $\mathcal{B}$ basis one finds the transformation of the U tensor:

$$\hat{O} = \sum_{mnop} \underbrace{\sum_{ijkl} T_{mi} T_{nj} U^{\mathcal{A}}_{ijkl} T^*_{pl} T^*_{ok}}_{=:U^{\mathcal{B}}_{mnop}} b_m^{\dagger} b_n^{\dagger} b_p b_o \tag{3.8}$$

3.2.2.1 Cubic basis

Our starting point for the DMFT calculation in TRIQS are the Wannier-projected Green's functions created by dmftproj. Thus our initial basis is set in `.indmftpr` file. For the scope of this work, the option `cubic` was chosen, so our starting basis is further on referred to as *cubic basis*. However, it is important to know that the definition of this basis follows a convention, such that:

---

[4] Of course $T^{\dagger} \equiv T^{\dagger}_{\mathcal{A}\to\mathcal{B}} = T_{\mathcal{B}\to\mathcal{A}}$

$$\begin{aligned}
d_{z^2} &= Y_2^0 \\
d_{x^2-y^2} &= \frac{1}{\sqrt{2}}(Y_2^{-2} + Y_2^2) \\
d_{xy} &= \frac{1}{\sqrt{2}}(Y_2^2 - Y_2^{-2}) \\
d_{xz} &= \frac{1}{\sqrt{2}}(Y_2^{-1} - Y_2^1) \\
d_{yz} &= \frac{1}{\sqrt{2}}(Y_2^1 + Y_2^{-1})
\end{aligned}$$

Note that unlike other common definitions, all of the basis functions are real valued, leading to a real valued transformation matrix T (from spherical to cubic)[5]:

$$T_{\text{sph}\to\text{cub}} = \begin{bmatrix} 0 & 0 & 1 & 0 & 0 \\ 1/\sqrt{2} & 0 & 0 & 0 & 1/\sqrt{2} \\ -1/\sqrt{2} & 0 & 0 & 0 & 1/\sqrt{2} \\ 0 & 1/\sqrt{2} & 0 & -1/\sqrt{2} & 0 \\ 0 & 1/\sqrt{2} & 0 & 1/\sqrt{2} & 0 \end{bmatrix} \tag{3.9}$$

It is also important to note that the only difference between the $d_{x^2-y^2}$ and d_{xy} basis function is a minus sign (ergo a phase factor). Therefore, after projecting using dmftproj, one should check which basis function represents the $t_{2\text{g}}$ orbitals.

3.2.2.2 Cubic basis with spin

In the presence of spin-orbit coupling and thus the removal of spin degeneracy, one has to consider ten basis functions with spin explicitely:

$$d^{\uparrow}_{z^2}, d^{\uparrow}_{x^2-y^2}, d^{\uparrow}_{xy}, d^{\uparrow}_{xz}, d^{\uparrow}_{yz} \quad \text{and} \quad d^{\downarrow}_{z^2}, d^{\downarrow}_{x^2-y^2}, d^{\downarrow}_{xy}, d^{\downarrow}_{xz}, d^{\downarrow}_{yz}$$

However, one can show (see section 2.1.2.2 and [22]) that under $\boldsymbol{L}\cdot\boldsymbol{S}$ coupling those ten basis functions decouple into two 5×5 blocks again (but now with mixed spin):

$$\underbrace{d^{\uparrow}_{z^2}, d^{\uparrow}_{x^2-y^2}, d^{\uparrow}_{xy}, d^{\downarrow}_{xz}, d^{\downarrow}_{yz}}_{=:\texttt{ud\_0}} \quad \text{and} \quad \underbrace{d^{\downarrow}_{z^2}, d^{\downarrow}_{x^2-y^2}, d^{\downarrow}_{xy}, d^{\uparrow}_{xz}, d^{\uparrow}_{yz}}_{=:\texttt{ud\_1}}$$

---

[5] This can be found in the HDF archive under `ar['dft_input']['T'][# of corr shell]`

SumkDFT can automatically find these blocks and sets the block structure accordingly:

```
SK = SumkDFT(my_hdf_file, use_dft_blocks = True) # either with
    ↪ use_dft_blocks

SK.analyse_block_structure() # or with analyse_block_structure
```

Listing 3.3 – Finding the block structure in SumkDFT

3.2.2.3 Reduced cubic basis

When the e_g orbitals lie significantly above the Fermi energy, one can take the approximation of doing the DMFT calculation using only the $t_{2\mathrm{g}}$ orbitals.

This can be done by changing the sumk_to_solver mapping in SumkDFT (thus not affecting any data in the HDF archive):

```
SK = SumkDFT(my_hdf_file)
interesting_indices_no = [2,3,4,7,8,9] # indices of t2g orbitals

SK.block_structure.pick_gf_struct_sumk([{'ud':
    ↪ interesting_indices_no}])
```

Listing 3.4 – Picking only t2g orbitals in SumkDFT

Note however that this is of course not a unitary transformation. This will become especially important later on, when transforming operators for observables (see section 3.2.2.5).

3.2.2.4 Diagonal basis

As stated in section 2.2.2.5, the sign problem can be a limiting factor in QMC calculations. However, as the average value of the sign is no physical expectation value, it does not have to be invariant under a basis transformation. This can be exploited if one can find a basis in which the average sign is maximized [22].

One good guess for such a basis is the eigenbasis of the problem's local Hamiltonian - which will be called *diagonal basis* on the following pages. To find this basis, the local Hamiltonian is diagonalized prior to the first DMFT iteration and the transformation matrix is stored in the HDF file.

Gernot Kraberger has written a python module called matrix_dict with which the diagonalization of H_loc and, further on, the transformation of Green's functions can be implemented very easily:

```
from matrix_dict import *

Hloc = eff_atomic_levels_solver(inverse(first_Sigma_cub +
    ↪ inverse(first_G_loc))) # extracting noninteracting Hloc
    ↪ from G0
e,V = Hloc.diagonalize()
V_full = V.to_full_matrix(gfs_cub.sumk_to_solver[0])
```

Listing 3.5 – Diagonalizing Hloc

3.2.2.5 Transformations in TRIQS

Transformation of the interaction tensor: With all transformation matrices defined, the question arises of how to actually transform Green's functions and other objects in TRIQS.

Starting with the interaction tensor U_{ijkl} for two-particle operators, TRIQS offers the function `transform_U_matrix(U_matrix, T)` (found in `pytriqs.operators.util`). However, the implementation of this function[6] differs from our chosen convention in equation (3.8). To be consistent with our definitions, we have to call this method with the conjugated transformation matrix.

```
from pytriqs.operators.util import *

# Generate interaction tensor in spherical basis
U_sph = U_matrix(l=2, U_int=U, J_hund=J) # 5x5
#  Blow up to two spins
U_sph = np.kron(np.reshape(np.eye(2),(1,2,1,2)),np.kron(np.
    ↪ reshape(np.eye(2),(2,1,2,1)),U_sph)) # 10x10

U_cub = transform_U_matrix(U_sph, SK.T[0].conjugate()) # call
    ↪ with T.conjugate()
U_dia = transform_U_matrix(U_cub, V_full.conjugate())
```

Listing 3.6 – Transformation of U matrix

Transformation of Green's functions: When transforming Green's functions two things have to be considered: The transformation itself, defined by the transformation matrix T, but also a possible change in the Green's function's structure. This might be the case when one wants to approximate the Green's function as diagonal[7] (turning the two 5×5 blocks into ten 1×1 blocks, removing all off-diagonal elements) in the diagonal basis.

---

[6] `np.einsum(”ij,kl,jlmo,mn,op”,np.conj(T),np.conj(T),U_matrix,np.transpose(T),np.transpose(T))`

[7] This can be easily done with SK.block_structure.approximate_as_diagonal()

Gernot Kraberger's `matrix_dict` module offers the method `rotate_and_convert_gf` ↪ that can do both in one step:

```
from matrix_dict import *

S.G_iw << rotate_and_convert_gf(Gloc, T, gfs_cub, gfs_diag, beta
    ↪ =beta)
```

Listing 3.7 – Transformation of Green's functions

Transformation of operators: For the transformation of second quantization operators there is (as of TRIQS 1.4) no preexisting method. The author of this thesis has implemented such a method (see Listing 3.9) and it will be commited to the TRIQS repository soon.

With this method, operators can be transformed like this:

```
# fops define the order of elements regarding rows and columns
    ↪ of the T matrix
fops_sph = [['UP','sp-2'], . . . ,['DN','sp+2']]
fops_dia = [['ud_0',0], . . . ,['ud_9',0]]

L2_diagonal = transform_operator(L2_spherical, T, fops_sph,
    ↪ fops_dia)
```

Listing 3.8 – Transformation of operators

3.2.3 "Hermitian Symmetrization" of Sigma

As introduced in section 2.1.4, equation (2.54), Matsubara Green's functions obey the symmetry relation

$$G_{ij}(i\omega) = G^*_{ji}(-i\omega) \tag{3.10}$$

However, this is not accounted for in the result of the CTHYB solver[8]. One can manually symmetrize the calculated Green's functions to avoid numerical errors. This turned out to be crucial, as otherwise small deviations in Sigma exaggerated themselves and no convergence could be reached.

```
for block, gf in S.Sigma_iw:
    gf.data[:,:,:] = (gf.data[:,:,:] + gf.data[::-1].transpose
    ↪ ([0,2,1]).conjugate())/2
```

Listing 3.10 – "Hermitian Symmetrization" of Sigma

---

[8] In fact it has been implemented in the latest version (2.1) of TRIQS in form of the `fit_hermitian_tail ()` function at least for the tail of the Green's function.

```
    r"""
    Transform an operator from one basis to another.

    .. math:: \hat O' = T \hat O T^\dagger

    Parameters
    ----------
    O_in : Operator
           Operator to be transformed
    T : real/complex numpy array
        Unitary transformation matrix (according to O' = T O T^\
   ↪ dagger
        Order of rows and columns according to fops_from and
   ↪ fops_to
    fops_from : List of lists
                Fundamental operator set in the original
   ↪ operator, e.g. [['up',0],['up',1],['dn',0],['dn',1]]
    fops_to : List of lists
              Fundamental operator set in the transformed
   ↪ operator

    Returns
    -------
    O_out : Operator
            The transformed operator
    """
def transform_operator(O_in, T, fops_from, fops_to):
    O_out = Operator(0)

    for monomial in O_in:
        coefficient = monomial[-1]
        new_monomial = Operator(1)

        for single_operator in monomial[0]:
            new_single_operator = Operator(0)
            daggered = single_operator[0]
            i = fops_from.index(single_operator[1])
            for j in range(len(fops_to)):
                new_single_operator +=  (T[j,i] * c_dag(*fops_to
   ↪ [j])) if daggered else (T[j,i].conjugate() * c(*fops_to[j
   ↪ ]))
            new_monomial *= new_single_operator

        O_out += new_monomial * coefficient
    return O_out
```

Listing 3.9 – transform_operator() method

3.2.4 DMFT Loop

Having defined all basis transformations, the DMFT loop itself is just going back and forth between the cubic basis (for SumkDFT) and the diagonal basis (for the solver). Instead of checking convergence after every loop, our calculations are set such that they run a pre-defined number of iterations, after which convergence should be checked manually. The corresponding flowchart can be found in Fig. 3.1.

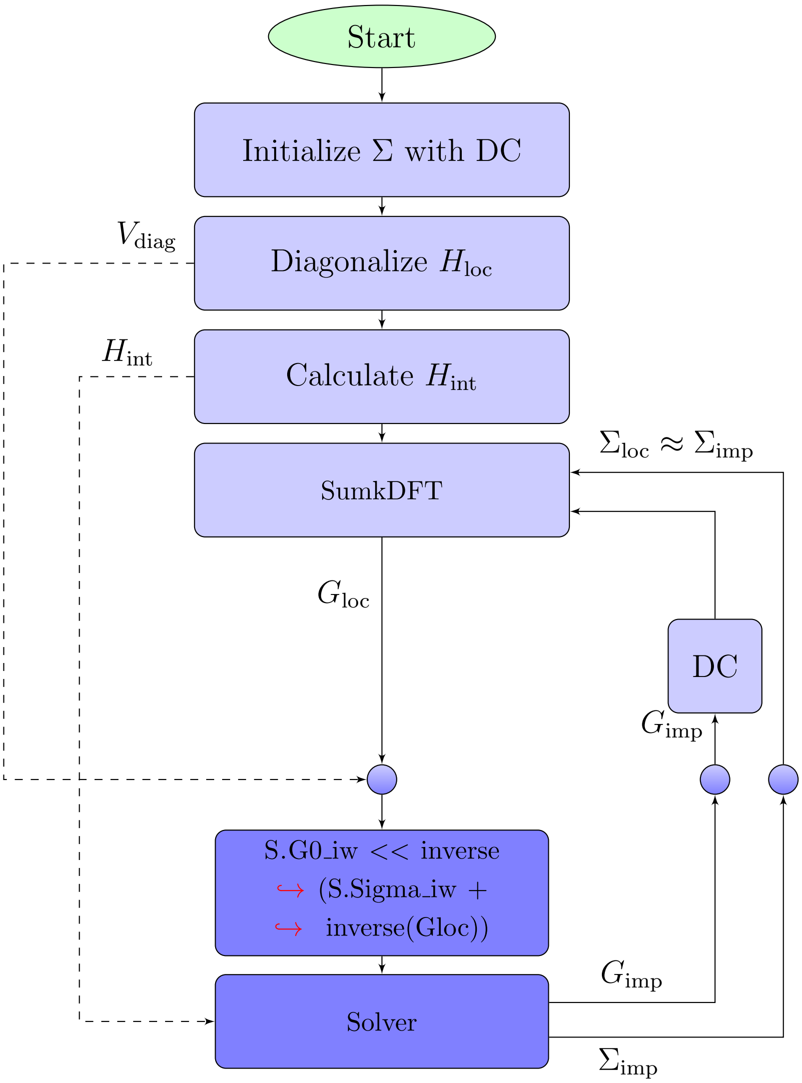
Start
Initialize Σ with DC
V_{diag}
Diagonalize H_{loc}
H_{int}
Calculate H_{int}
$\Sigma_{\text{loc}} \approx \Sigma_{\text{imp}}$
SumkDFT
G_{loc}
DC
G_{imp}
S.G0_iw << inverse
↪ (S.Sigma_iw +
↪ inverse(Gloc))
G_{imp}
Solver
Σ_{imp}

Figure 3.1 – Flowchart of the DMFT loop in TRIQS.
The small circles indicate basis transformations, the darker blue color indicates the diagonal basis.

3.2.5 Observables and expectation values

The expectation value of an operator can be calculated from the density matrix ρ using the known relation

$$\left\langle \hat{O} \right\rangle = \mathrm{Tr}\left\{ \hat{\rho} \cdot \hat{O} \right\} \tag{3.11}$$

The many-body density matrix of the systen can be measured during a DMFT loop by the CTHYB solver. As the solver searches for symmetries to reduce Hilbert space dimension, the density matrix falls apart into various blocks of different size (the `density_matrix` object is a list of length $\#_{\text{Symmetries}}$ with list entries being $n \times n$ arrays, the density matrices of the single blocks). The structure of the blocks is stored in a `h_loc_diagonalization` object that is also created by the solver. Equation (3.11) can then be evaluated using `trace_rho_op(density_matrix, O, h_loc_diag)`.

```
from pytriqs.applications.impurity_solvers.cthyb import *

p[”measure_density_matrix”] = True
p[”use_norm_as_weight”] = True

S = Solver(. . .)
S.solve(h_int = H, **p)

rho = S.density_matrix
h_loc = S.h_loc_diagonalization

expval = trace_rho_op(rho, my_operator, h_loc)
```

Listing 3.11 – Measurement of density matrix and exp. values in CTHYB

3.2.5.1 Orbital angular momentum

TRIQS offers methods to implement the orbital angular momentum operators introduced in equation (2.7). For the general usage of the methods `L_op( . . . )` and `L2_op( . . . )` one is best referred to the TRIQS documentation. In this paragraph some special considerations when using these methods in the scope of the reduced cubic basis (introduced in section 3.2.2) are presented.

As we neglect the e_g orbitals for the calculations in this work, the angular momentum operators for the t_{2g} manifold ($l = 2$) can be calculated from the p operators ($l = 1$) using the T-P equivalence (introduced in section 2.1.1.2)

Note that the `spherical_to_cubic(l=1)` function does not use the same convention as introduced in equation (2.13). To get the right transformation matrix, one has to multiply it with the `swap_indizes` matrix from listing 3.12 (or simply type in the matrix from (2.13) by hand).

```
xyz = ['x','y','z']
L_p = map(lambda k: L_op(xyz[k],['UP','DN'],[-1,0,1],off_diag =
    ↪ True, basis = 'spherical'),(0,1,2))

T_full = np.kron(np.eye(2,2,),spherical_to_cubic(l=1))
swap_indizes = np.kron(np.eye(2,2),np.matrix([[0,0,1j
    ↪ ],[0,1,0],[-1j,0,0]]))
U_tp = np.dot(swap_indizes,T_full)

fops_tp_SPH = [['UP',-1],['UP',0],['UP',1],['DN',-1],['DN',0],['
    ↪ DN',1]]
fops_tp_cub = [('ud_0',0),('ud_1',0),('ud_1',1),('ud_1',2),('
    ↪ ud_0',1),('ud_0',2)]
L_tp = map(lambda k: -transform_operator(L_p[k],U_tp,
    ↪ fops_tp_SPH, fops_tp_cub),(0,1,2)) # note the minus sign
```

Listing 3.12 – L operator via T-P equivalence

The same result can be achieved by removing the e_g operators from the full $l = 2$ orbital angular momentum operator. However, as mentioned in section 3.2.2.3 (reduced cubic basis), this is no unitary transformation, so one has to take care at which point the operators are removed.

In fact, the e_g operators have to be removed in the components of the $\boldsymbol{L}$ operator (L_x, L_y, L_z), before being multiplied together for the $L^2 = L_x^2 + L_y^2 + L_z^2$ operator, as in the second case TRIQS automatically simplifies the expression by evaluating terms such as $c_i c_i^\dagger = 1 - c_i^\dagger c_i$.

When comparing these operators, one can look at the diagonal elements of the L^2 operator: The full-d operator has diagonal values of 6 (as expected for a $l = 2$ operator[9]) whereas the t_{2g}-only operator has diagonal values of 2 (like a $l = 1$ operator).

```
fops_sph = [['UP','sp-2'],['UP','sp-1'],['UP','sp0'],['UP','sp+1
    ↪ '],['UP','sp+2'],['DN','sp-2'],['DN','sp-1'],['DN','sp0'
    ↪ ],['DN','sp+1'],['DN','sp+2']]
fops_cub = [('eg1',0),('eg2',0),('ud_0',0),('ud_1',0),('ud_1',1)
    ↪ ,('eg3',0),('eg4',0),('ud_1',2),('ud_0',1),('ud_0',2)]


L_sph = {}
L_cub = {}

xyz = ['x','y','z']
```

---

[9] $L^2 \left|l, m_l\right\rangle = \hbar^2 l(l+1) \left|l, m_l\right\rangle$

```
for comp in xyz:
    L_sph[comp] = L_op(comp,spin_names=['UP','DN'], orb_names=['
    ↪ sp-2','sp-1','sp0','sp+1','sp+2'], off_diag=True)
    L_cub[comp] = transform_operator(L_sph[comp], T_full,
    ↪ fops_sph, fops_cub)

    # Remove the eg operators for every component
    L_cub[comp] = remove_all_eg_operators(L_cub[comp])
```

Listing 3.13 – L operator with removed eg orbitals

The `remove_all_eg_operators()` method used above has to be implemented to fit the orbital and spin naming convention of the problem at hand. One example for the convention used above can be found in Listing 3.14.

```
def remove_all_eg_operators(operator_in):
    new_total_operator = Operator(0)
    for op_part in operator_in:

        new_part_operator = Operator(1)
        coefficient = op_part[-1]

        for single_operator in op_part[0]:
            daggered = single_operator[0]

            # This line has to be changed
            # depending on naming convention
            if single_operator[1][0].startswith('eg'):
                new_part_operator = Operator(0)
                continue
            new_part_operator *= c_dag(*single_operator[1]) if
    ↪ daggered else c(*single_operator[1])
        new_part_operator *= coefficient
        new_total_operator += new_part_operator

    return new_total_operator
```

Listing 3.14 – `remove_all_eg_operators()` method

3.2.5.2 Spin angular momentum

The spin angular momentum operators are easy to calculate in a basis where the blocks correspond to the physical spins. However, as we have seen in section 3.2.2.2 (cubic basis with spin), this is not the case for our cubic basis with SOC, as the blocks `ud_0` and `ud_1` mix the physical spins (`UP` and `DN`).

However, as there is no 'real' transformation done in section 3.2.2.2 (just a renaming and reordering of the basis), we can simply 'transform' the operator by choosing suitable fundamental operator sets as can be seen in the following listing:

```
comps = ['z','x','y']

fops_spin = [['UP', 0],['UP', 1],['UP', 2],['UP', 3],['UP',
    ↪ 4],['DN', 0],['DN', 1],['DN', 2],['DN', 3],['DN', 4]]
fops = [['eg1',0],['eg2',0],['ud_0',0],['ud_1',0],['ud_1',1],['
    ↪ eg3',0],['eg4',0],['ud_1',2],['ud_0',1],['ud_0',2]]

for comp in comps:
    Sop[comp] = S_op(comp,spin_names=['UP','DN'], orb_names
    ↪ =[0,1,2,3,4], off_diag=True)
    Sop_cub[comp] = transform_operator(Sop[comp], np.eye(10,10),
    ↪  fops_spin, fops) # renaming the spin-blocks
    Sop_cub[comp] = remove_all_eg_operators(Sop_cub[comp])
```

Listing 3.15 – S operator

3.2.5.3 Total angular momentum

The total angular momentum $\boldsymbol{J}$ is given by

$$\boldsymbol{J} = \boldsymbol{L} + \boldsymbol{S} \tag{3.12}$$

As known from basic quantum mechanics (e.g. [18]), for a system of multiple spins, one can find the "good" quantum numbers J^2, J^z, L^2, S^2. Of course, for J^2 follows

$$\boldsymbol{J}^2 = (\boldsymbol{L} + \boldsymbol{S})^2 = \boldsymbol{L}^2 + \boldsymbol{S}^2 + 2(\boldsymbol{L} \cdot \boldsymbol{S}) \tag{3.13}$$

When using the T-P equivalence from equation (2.15), one has to consider just the threefold d_{t2g} subspace (sixfold with spin), which corresponds to the p orbitals:

$$\boldsymbol{J}_{eff} \equiv \boldsymbol{J}_p = \boldsymbol{L}_p + \boldsymbol{S} \underset{\text{T-P equiv.}}{=} -\boldsymbol{L}_{t2g} + \boldsymbol{S} \tag{3.14}$$

For the J^2 operator, this means:

$$\boldsymbol{J}_{eff}^2 = \boldsymbol{L}_{t2g}^2 + \boldsymbol{S}^2 - 2(\boldsymbol{L}_{t2g} \cdot \boldsymbol{S}) \tag{3.15}$$

Thus, the sign of the $\boldsymbol{L} \cdot \boldsymbol{S}$ term has to be changed when using the T-P equivalence.

3.2.6 AFM calculations

3.2.6.1 Transformation of the inequivalent sites

As both inequivalent magnetic sites are in fact equivalent in absence of magnetic ordering, a transformation can be found to calculate G^B_{loc} from G^A_{loc} (A, B being the two different sites).

However, there can be an arbitrary phase shift between the two sites [53] introduced during the projection in dmftproj. One can either try finding a "simple" transformation by hand (by comparing the two G_0s), or use Gernot Kraberger's analyse_deg_shells script to automatically find a transformation from one site to the other.

Such a transformation T can be written in block-diagonal form, as it does not mix spins (here $\uparrow$ and $\downarrow$ indicate the different decoupled spin-blocks, which do not have to coincide with the physical spins):

$$G^B_{\text{loc}} = T G^A_{\text{loc}} T^\dagger \tag{3.16}$$

$$T = \begin{bmatrix} T^\uparrow & 0 \\ 0 & T^\downarrow \end{bmatrix} \tag{3.17}$$

In the same manner, one can find a transformation linking the two decoupled spin-blocks with each other. For a paramagnetic system ($G^\uparrow \equiv G^\downarrow$) in a suitable basis, this transformation S can be trivially written as

$$S = \begin{bmatrix} 0 & \mathbb{1} \\ \mathbb{1} & 0 \end{bmatrix} \tag{3.18}$$

Once both of these transformations are found, the anti-ferromagnetic model can be calculated by just solving one impurity and then transforming the result to the second impurity using a product of spin-flip transformation S (3.18) and site transformation T (3.17):

$$G^B_{\text{imp}} = (TS) G^A_{\text{imp}} (TS)^\dagger \tag{3.19}$$

$$TS = \begin{bmatrix} 0 & T^\uparrow \\ T^\downarrow & 0 \end{bmatrix} \tag{3.20}$$

3.2.6.2 AFM DMFT loop

With all of the above in the back of our head, we can now go ahead and extend the TRIQS DMFT-loop (Fig. 3.1) to anti-ferromagnetic systems. The changes to be made are initializing Σ with a polarization in the spins (otherwise, one would run into a meta-stable paramagnetic solution), solve the AIM for one site, calculating the second site using equation (3.19) and finally calculate DC for both sites. The resulting anti-ferromagnetic DMFT loop can be found in Fig. 3.2.

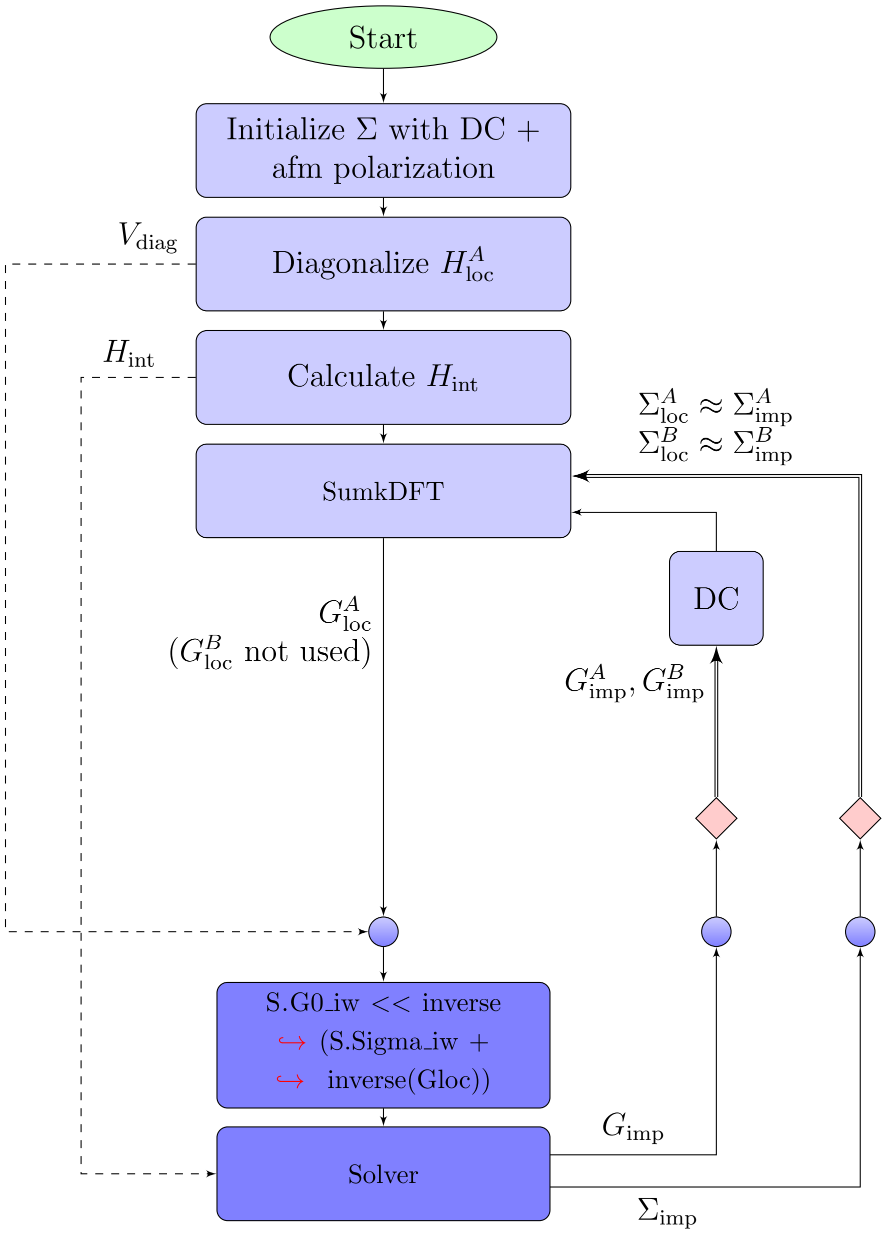
Start
Initialize Σ with DC + afm polarization
Diagonalize H_{loc}^A
V_{diag}
Calculate H_{int}
H_{int}
SumkDFT
$\Sigma_{\text{loc}}^A \approx \Sigma_{\text{imp}}^A$
$\Sigma_{\text{loc}}^B \approx \Sigma_{\text{imp}}^B$
DC
G_{loc}^A
(G_{loc}^B not used)
$G_{\text{imp}}^A, G_{\text{imp}}^B$
S.G0_iw << inverse
↪ (S.Sigma_iw +
↪ inverse(Gloc))
Solver
G_{imp}
Σ_{imp}

Figure 3.2 – Flowchart of the AFM DMFT loop in TRIQS.
The small circles indicate basis transformations, the darker blue color indicates the diagonal basis, red diamonds indicate doubling of the Green's function (Eqn. (3.19)).

Chapter 4

Application to Ba_2YIrO_6

The tools laid out in the previous chapters are now applied to Ba_2YIrO_6 (BYIO) introduced in section 1.2. First its paramagnetic behaviour is investigated, then possible long-range ordering of magnetic moments is analyzed.

4.1 Paramagnetic System

4.1.1 Structure

The struct files for the DFT calculations were taken from [9] via the ICSD database (see Fig. 4.1). However, upon inspection it became obvious that the coordinates of the Ir and Y atoms were mistaken one for another in [9] (otherwise the Ir-O and Y-O distances given in [9] were not correct and did not correspond to the atom's ionic radii).

To confirm this suspicion, the DFT calculations were run both with the (wrong) ICSD struct file and the corrected struct file (where the coordinates for the Ir and Y atoms were exchanged). The corrected struct file led to a lower ground state energy.

4.1.2 DFT + dmftproj

4.1.2.1 DFT band structure

The DFT calculations were performed using Wien2k [48] and the PBE potential [29]. The calculations were run spin-polarized and both with and without spin-orbit coupling. The number of k-points in the full Brillouin zone was chosen at 10.000 (see section 4.2.1 for info about k-point convergence). The resulting band structure plot can be found in Fig. 4.2.

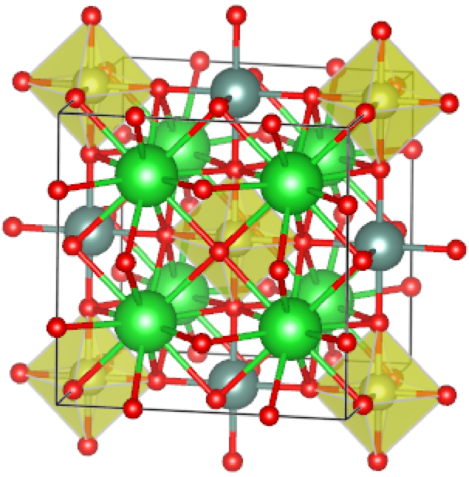

Figure 4.1 – Double perovskite crystal structure of Ba$_2$YIrO$_6$.
In green the Ba atoms, grey the Y atoms, red the O atoms and yellow the Ir atoms with their oxygen-octahedra are shown.

The DFT results clearly show a metallic behaviour, which will be lifted when introducing interactions via DMFT. A orbital character plot (Fig. 4.3) of the calculation including spin-orbit coupling shows mainly Ir-t_{2g} character around the Fermi level. It is also apparent that the crystal-field splitting $\Delta_{CF} \approx 3$ eV is quite large, allowing the approximation of considering t_{2g} and e_g to be decoupled.

4.1.2.2 Magnetic moment

First, a regular spin-polarized calculation was done to determine the magnetic moment in DFT. The results can be found in Tab. 4.1. The total magnetic moment coincides with the results found in [13] (the partial magnetic moments of the atom's muffin-tin-spheres depend on the chosen basis and muffin-tin-radii and thus cannot be compared).

Table 4.1 – Magnetic moment of BYIO in DFT
(Int. = Interstitial)

	Int.	Ba	Y	Ir	O	total
μ / μ_b	0.157	0.005	-0.003	0.538	0.117	1.07

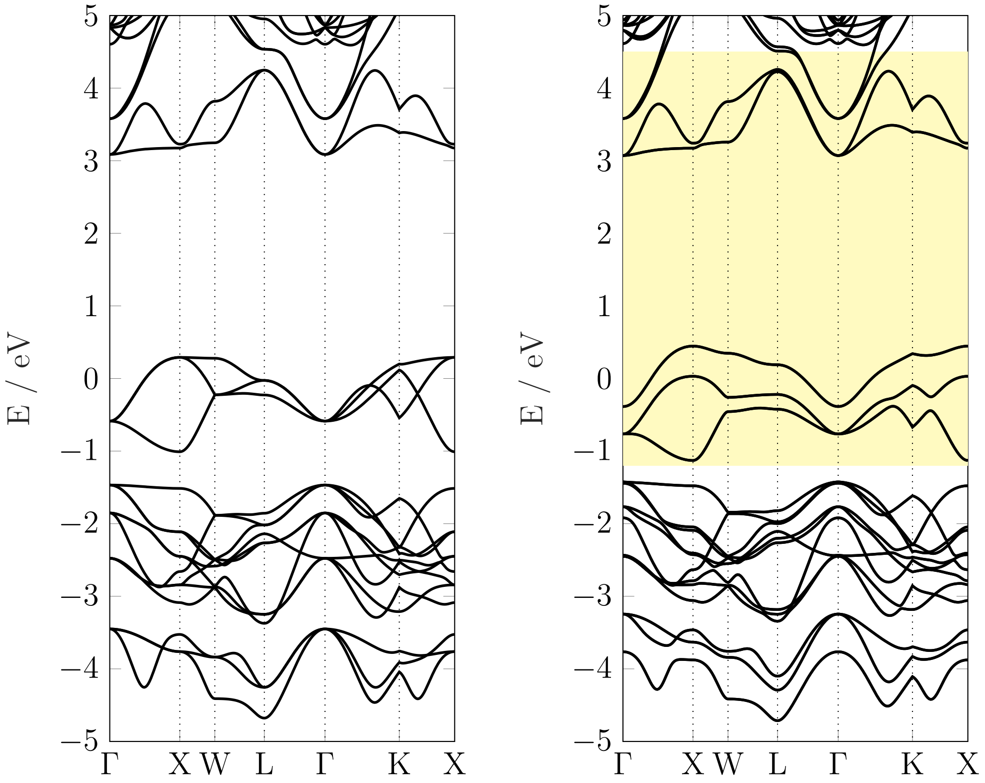

(a) without SOC **(b)** with SOC

Figure 4.2 – DFT band structure for BYIO
In yellow the chosen projection window $\mathcal{W}$.
The apparent metallic behaviour will be lifted with the introduction of interactions in the framework of DMFT (metal-insulator transition).

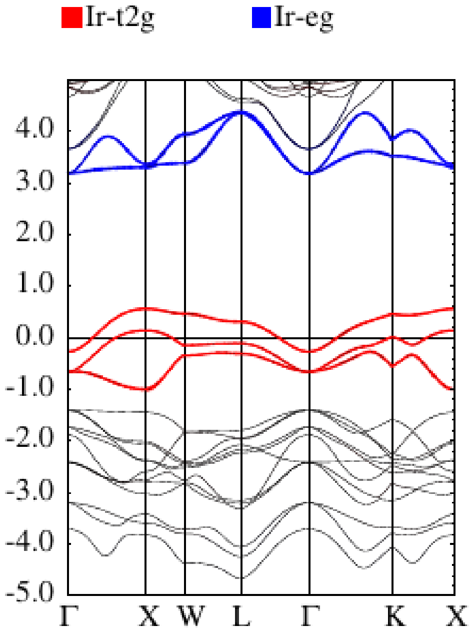

Figure 4.3 – DFT orbital character plot for BYIO with spin-orbit coupling.

4.1.2.3 dmftproj

As basis for the DMFT calculation a spin-polarized calculation with forced zero magnetic moment was performed both with and without SOC. Then dmftproj was used on the calculation including SOC, projecting the Bloch bands onto the localized Wannier orbitals of the Ir atoms. For this, a window containing the full Ir d-shell was chosen ($\mathcal{W} = [-0.09, 0.33]$ Ry $= [-1.2, 4.5]$ eV, see Fig. 4.2b), as a 'cut' through the d-bands (in between t_{2g} and e_g) and thus a projection of just the t_{2g} manifold would throw away small hybridisation elements introduced by the SOC (see next paragraph and Fig. 4.4). This presence of SOC also made a splitting into ireps impossible.

The DOS in the projected basis (including the off-diagonal elements introduced by the spin-orbit coupling) for the paramagnetic structure can be found in Fig. 4.4. It can be seen that while the off-diagonal elements between t_{2g} and e_g are small, they are in fact not zero. However, they are of order $\mathcal{O}(10)$ smaller than the elements within the t_{2g} manifold, so we will approximate t_{2g} and e_g to be decoupled.

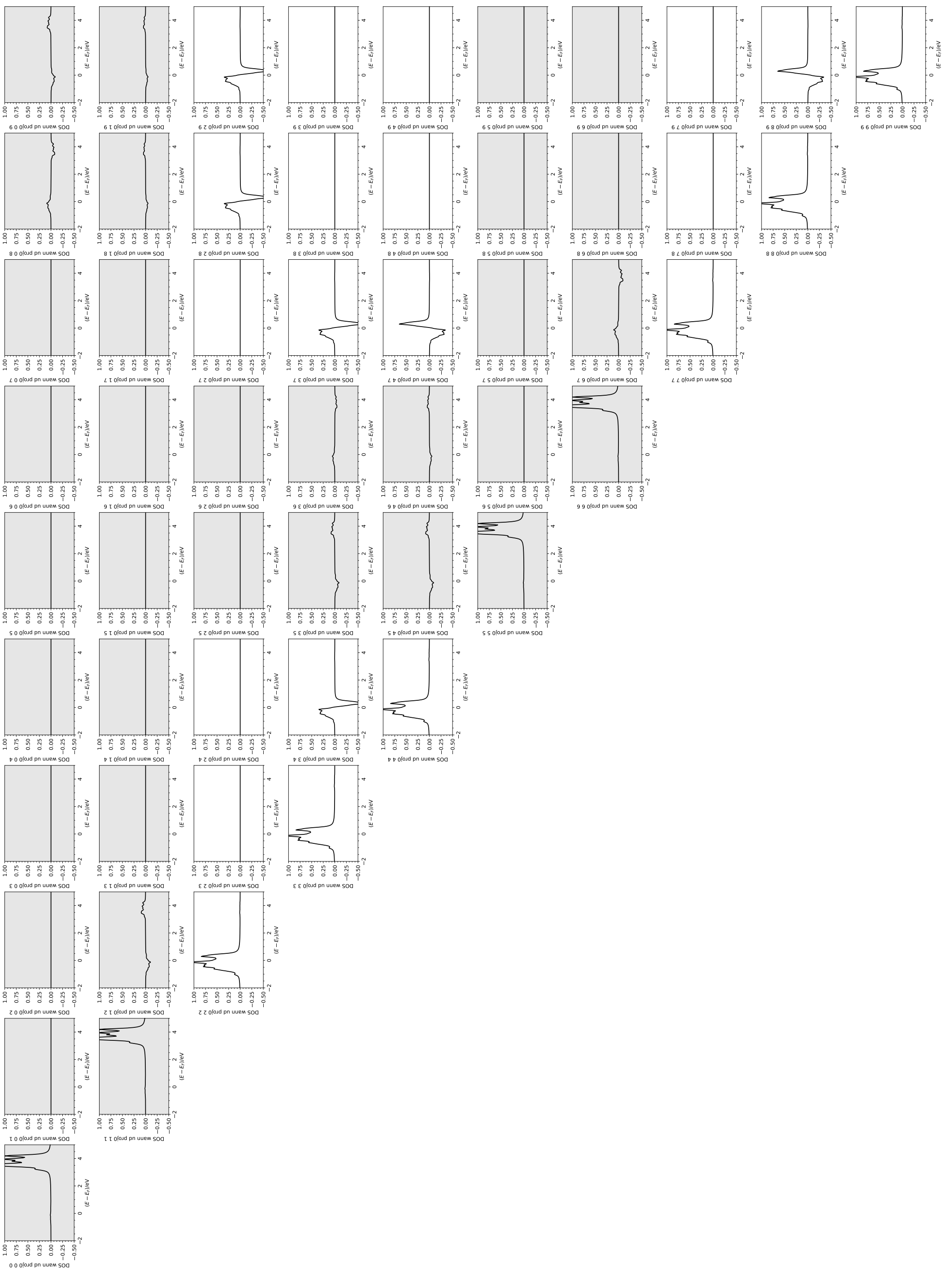

Figure 4.4 – DOS projected onto Wannier orbitals (PM structure) in cubic basis. The first 5 rows correspond to spin up, the last 5 to spin down. The e_g orbitals and the corresponding off-diagonal elements are grayed out.

4.1.3 DMFT

Due to the large crystal-field splitting in the order of 3 eV, the e_g orbitals were omitted for the calculation. For the interaction a full Slater-type Hamiltonian with $U = 2$ eV and $J = 0.3$ eV was chosen (cRPA calculations [12] lead to $U = 1.8$ eV and $J = 0.4$ eV for their d-model). For the first calculations the temperature was set at $\beta = 40\ \mathrm{eV}^{-1}$ (≈ 290 K).

4.1.3.1 Diagonalizing H_loc

To improve the average sign of the QMC solver, the calculations were performed in the diagonal basis (where H_loc is diagonal, see section 3.2.2.4). The corresponding transformation matrix from cubic to diagonal basis was found to be (e_g orbitals omitted, order of basis $d^\uparrow_{xy}, d^\uparrow_{xz}, d^\uparrow_{yz}, d^\downarrow_{xy}, d^\downarrow_{xz}, d^\downarrow_{yz}$):

$$T_{\mathrm{cub}\to\mathrm{dia}} = \begin{bmatrix} \approx 0 & 0 & 0 & 0 & 0.707 & -0.707 \\ 0 & 0.707 & 0.707 & \approx 0 & 0 & 0 \\ 0 & -0.409 & 0.409 & -0.816 & 0 & 0 \\ 0 & -0.577 & 0.577 & 0.578 & 0 & 0 \\ 0.816 & 0 & 0 & 0 & 0.409 & 0.409 \\ -0.578 & 0 & 0 & 0 & 0.577 & 0.577 \end{bmatrix} \tag{4.1}$$

In other literature, this basis (where H_loc is diagonal) is often referred to as numerical j-basis. What is surprising is that in our case this basis matches with the effective j-basis introduced in equation (2.34) (apart from numerical inaccuracies - '≈ 0' meaning $\mathcal{O}(10^{-6})$ and order of basis).

Transforming the local DFT Green's function in real frequencies $G_\mathrm{loc}(\omega)$ into this diagonal basis leads to vanishing off-diagonal elements (see Fig. 4.5). As H_loc, per definition, is diagonal in our chosen basis, the same holds true for the hybridisation function $\Delta(\omega) = \omega - G^{-1}_\mathrm{loc}(\omega) - H_\mathrm{loc}$, as can be seen in Fig. 4.6. As we are using a hybridisation-expansion based solver (CTHYB), this means we are effectively calculating in a completely decoupled basis consisting of six 1×1 blocks with no off-diagonal elements in between.

4.1.3.2 Tail fitting

As the error in CTHYB-calculated self-energies scales roughly with $|\omega_n|^2$ [22], the MC data is only reliable for small frequencies. For higher frequencies one commonly used method is to fit the (noisy) data with a Laurent expansion up to a certain order.

One way to do so is to chose a fitting window $\mathcal{F} = [n_1, n_2]$ in which the fit is performed. Data for Matsubara fequencies lower than ω_{n_1} is not noisy

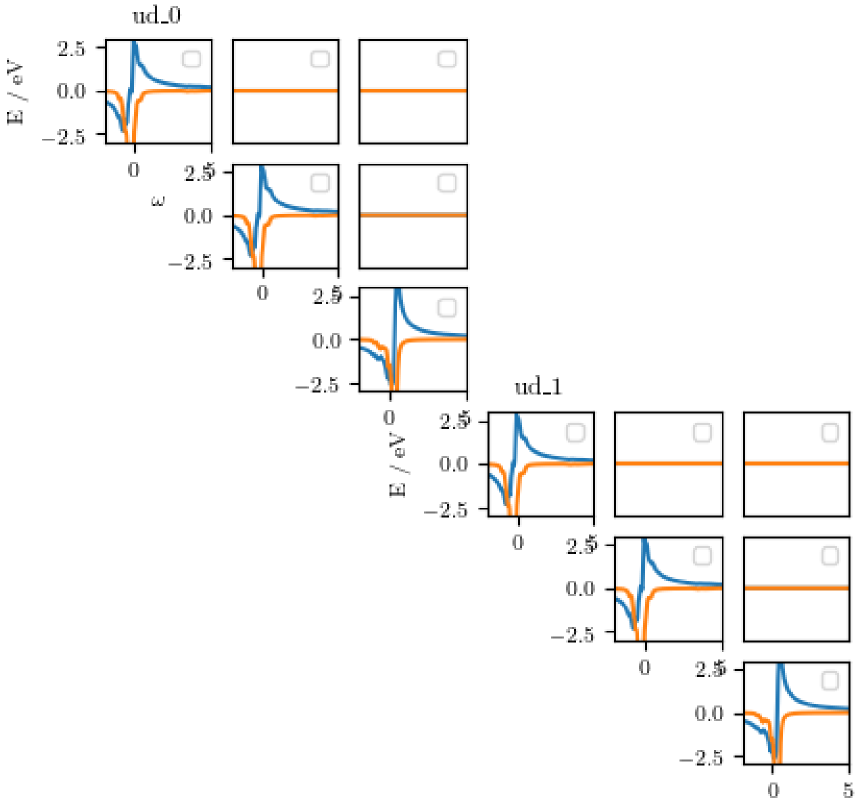

Figure 4.5 – $G_{\mathrm{loc}}(\omega)$ in the diagonal basis before the first iteration. Real part in orange, imaginary part in blue.

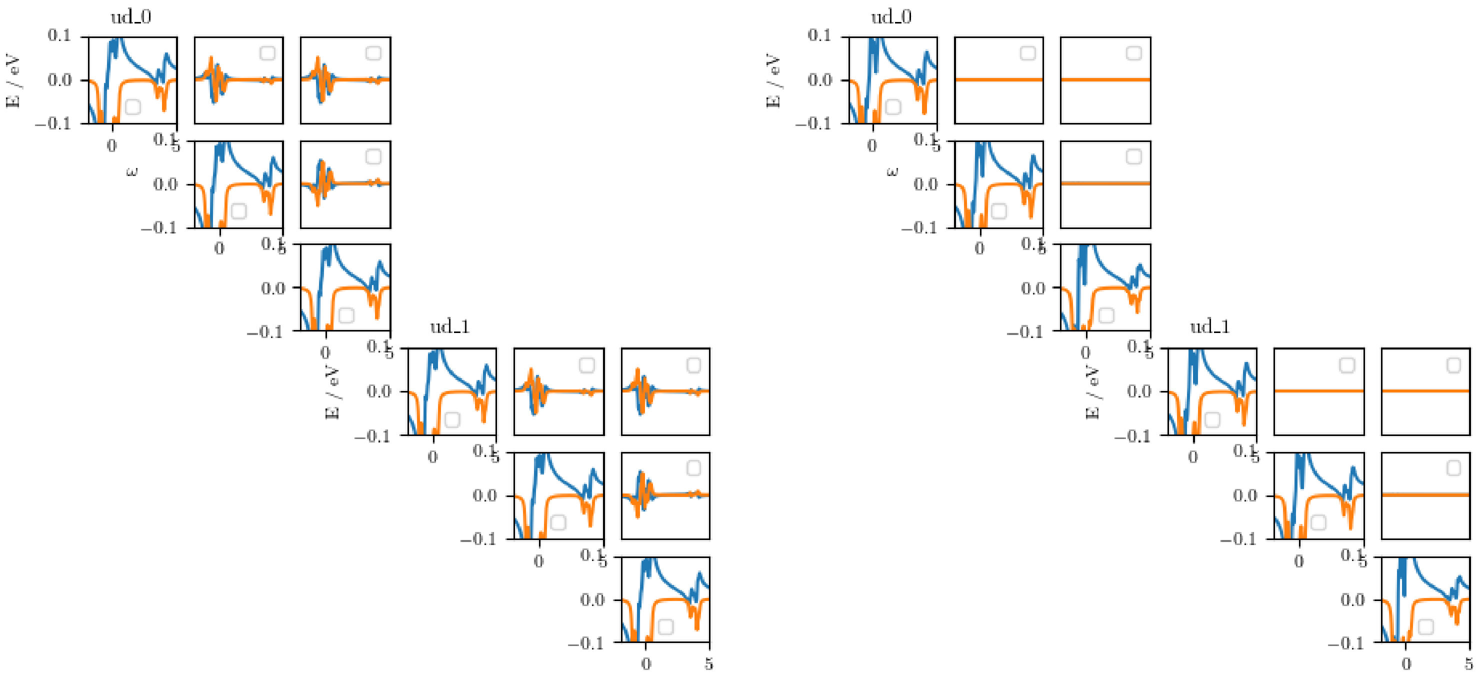

(a) Cubic basis

(b) Diagonal basis

Figure 4.6 – Hybridisation function $\Delta(\omega)$ before and after diagonalisation. Real part in orange, imaginary part in blue.

and does not follow the declining behavior of the fit [22]. Data above ω_{n_2} is too noisy to perform a meaningful fit. Thus the quality and results of the fit depends on the chosen n_1, n_2.

In order to get rid of at least the dependence on n_2, one can exploit that the error in $\Sigma(i\omega_n)$ increases quadratically. Therefore one can omit the upper bound of the fitting window, by minimizing $\chi^2 = \sum_n (\frac{f(i\omega_n)-\Sigma(i\omega_n)}{|(i\omega_n)^2|})^2$ which goes to zero for high frequencies [22]. This is the approach taken for this work. The fit was performed up to 4^{th} order, starting at the 20^{th} Matsubara frequency.

4.1.3.3 Metal-Insulator transition

The DMFT loop was run for 25 iterations, however after 10 iterations no more significant changes in the resulting self-energy were observed.

As $\mathrm{Im}\{G(i\omega_n \to 0)\} \propto A(\omega = 0)$, by looking at the imaginary part of the impurity's Green's function $G_{\mathrm{imp}}(i\omega_n)$ a clear metal-insulator transition can be observed (see Fig. 4.7).

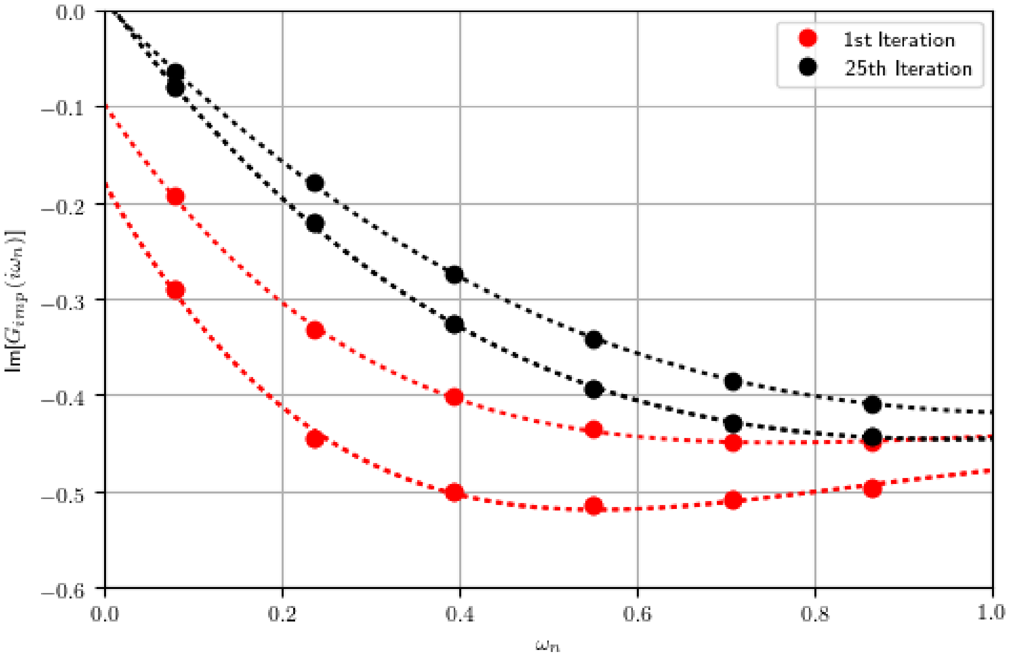

Figure 4.7 – $\mathrm{Im}[G_{\mathrm{imp}}(i\omega_n)]_{ii}$ on the first six Matsubara frequencies from the first iteration (red) and 25th iteration (black). The dashed lines are polynomial fits (of fourth order) over the first 10 Matsubara frequencies. A clear Metal-Insulator transition can be seen.

4.1.3.4 Observables

After convergence was reached, one more iteration was calculated, this time measuring the density matrix (see section 3.2.5). With this, the expectation values of $\langle L^2\rangle$, $\langle S^2\rangle$, $\langle LS\rangle$ and $\langle J^2\rangle$ were calculated. For comparison the same expectation values were calculated using an atomic limit solver (TRIQS' AtomDiag solver). The results can be found in Tab. 4.2.

Table 4.2 – Expectation values of the different observables for DMFT calculation at $\beta = 40$ eV^{-1} (with CTHYB) and atomic model (AD)
$U = 2$ eV, $J_{\text{Hund}} = 0.3$ eV
$J^2 = L^2 + S^2 - 2LS$ (see section 3.2.5.3)

	$\langle N\rangle$	$\langle L^2\rangle$	$\langle S^2\rangle$	$\langle LS\rangle$	$\langle J^2\rangle$
DMFT	3.97	1.85	1.85	1.76	0.19
AD	3.99	1.86	1.86	1.86	0.00

To investigate the temperature stability of the DMFT results, calculations at various values of β were performed. For each values of β, 15 iterations were calculated to reach convergence. The results can be found in Tab. 4.3. It can be seen that the expectation value for $\langle J^2\rangle$ does not change in the considered temperature range. Regardless of temperature, the $J_{\text{eff}} = 0$ state is not achieved for the DMFT lattice model.

Furthermore, the influence of the interaction parameter U was investigated. Therefore the calculations were performed at three different values of $U = \{1, 2, 6\}$ eV with $J_{\text{Hund}} = 0.15 \cdot U$. For each value of U the occupations of the $J_{\text{eff}} = 1/2$ and $J_{\text{eff}} = 3/2$ orbitals as well as the expectation values of $\langle J^2\rangle$ were measured. The results can be found in Tab. 4.4.

4.1.3.5 Spectral function

From the imaginary-frequency Green's function $G_{\text{loc}}(i\omega_n)$ the real-frequency Green's function $G_{\text{loc}}(\omega)$ and thus the spectral function

$$A(\omega) = -1/\pi \, \text{Im}\{G_{\text{loc}}(\omega)\} \tag{4.2}$$

Table 4.3 – Temperature dependence of $\langle J^2\rangle$ in DMFT
$U = 2$, $J_{\text{Hund}} = 0.3$

β / eV^{-1}	40	60	80	100	120
T / K	290	193	145	116	97
$\langle J^2\rangle$	0.19	0.19	0.19	0.19	0.19

Table 4.4 – U-dependence of $\langle J^2 \rangle$ and densities

U	$n_{3/2}$	$n_{1/2}$	$\langle J^2 \rangle_{DMFT}$	$\langle J^2 \rangle_{AD}$
1	0.96	0.07	0.36	0.00
2	0.94	0.11	0.19	0.00
6	0.88	0.23	0.08	0.00

can be calculated using analytic continuation [54]. However, as this poses an ill-defined problem, this is not straightforward and different computational methods have been developed. Here, a MaxEnt-based formalism [52] was used on the Green's function in the diagonal basis (thus no off-diagonal elements had to be considered). Also the DFT DOS in the Wannier basis (Fig. 4.4) was transformed into the (numerical) j-basis, giving the densities of the (non-interacting) DFT $J_{\text{eff}} = 1/2$ and $J_{\text{eff}} = 3/2$ orbitals. The effect of the interaction parameter $U = 2$ eV (coming from the cRPA calculations) on the DFT DOS can be found in Fig. 4.8, the influence of a varying interaction parameter in Fig. 4.9.

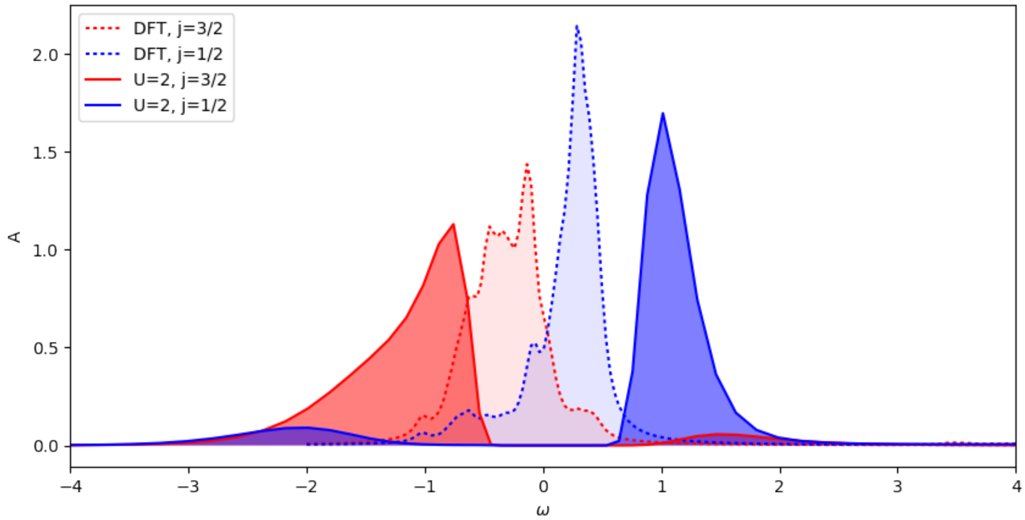

Figure 4.8 – Influence of the interaction parameter $U = 2$ ($J_{\text{Hund}} = 0.3$) on the DOS of BYIO.

Looking at Fig. 4.8 it can be seen that both with and without interactions the $J_{\text{eff}} = 1/2$ orbital gets partly occupied. For the DFT result this can also be seen in Fig. 4.2b as the highest t_{2g} band intersects the Fermi level. Thus it can be said, that the SOC is not strong enough to completely split the $J_{\text{eff}} = 1/2$ and $J_{\text{eff}} = 3/2$ manifolds in the band-structure picture. The

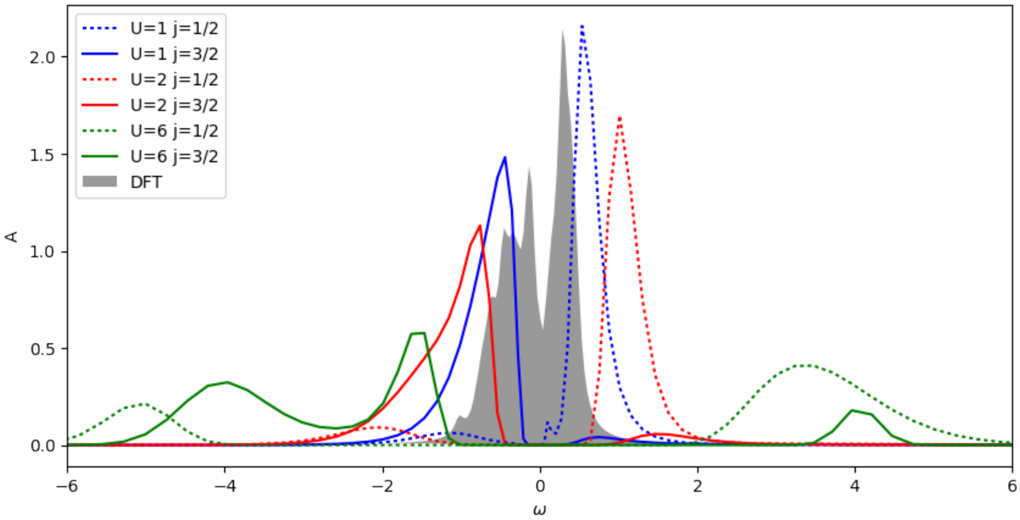

Figure 4.9 – Influence of various interaction parameters U ($J_{\text{Hund}} = 0.15 \cdot U$) on the spectral function.

observed metal-insulator transition is then a Mott transition happening in both orbitals.

In the limit of large interaction parameters U the calculation goes towards a $J_{\text{eff}} = 0$ state both for the atomic model as well as the DMFT model. This can be interpreted as a Van Vleck type magnet, where both $L = 1$ and $S = 1$ however $J = 0$ (the measured expectation values are $\langle L^2 \rangle = \langle S^2 \rangle = 1.97$, $\langle J^2 \rangle = 0.08$ for $U = 6$ eV).

4.2 Antiferromagnetic System

To investigate the possible long-range magnetic ordering observed by Terzic *et al.* (”Long-range magnetic order below 1.7 K is confirmed.”) [11] and disconfirmed by Dey *et al.* (”For temperatures down to 0.4 K long-range magnetic order is absent.”) [5] an anti-ferromagnetic DMFT calculation was performed.

4.2.1 Structure

The Ir atoms in BYIO’s double perovskite structure are aligned in an fcc-like structure. Thus, different anti-ferromagnic configurations can be realized. The supplementary material of [13] suggests that ”Type I” (see Fig. 4.10) has the lowest energy, therefore only this structure has been investigated. The antiferromagnetic struct file for the DFT calculation was generated by blowing up the simple paramagnetic struct file intruduced in section 4.1.1, creating a bigger supercell with two (magnetically) inequivalent Ir atoms.

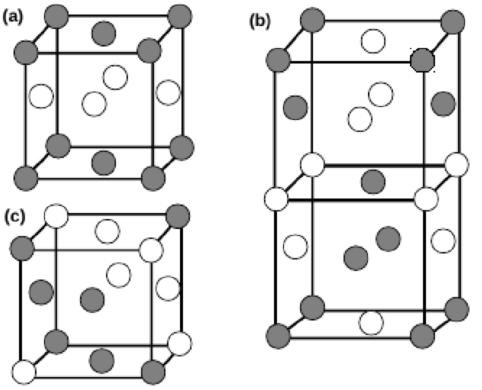

Figure 4.10 – Anti-ferromagnetic configurations for fcc-like structures. The circles represent the magnetic atoms (Ir). For this calculations Type I (a) has been chosen.
Taken from [13, Suppl. Material].

4.2.2 DFT

Out of curiosity, a k-point convergence calculation was performed[1], showing that the energy did not change significantly anymore after reaching about

---

[1] As our DFT calculations are computationally far less expensive as the following DMFT calculations, k-point convergence is normally skipped and a sufficiently large number of k-points is chosen.

1.000 k-points. Thus a k-point number well above that value (10.000) was chosen. It was also necessary to significantly tighten the convergence criterion of the DFT loop to gain equivalence of the non-magnetic Green's functions on the two Ir atoms. For this purpose, Wien2k's charge convergence parameter was set at $-$cc 0.00000001 (10^{-8}).

First a spin-polarized DFT calculation was performed, the resulting (spin-resolved) DOS can be found in Fig. 4.11. As basis for the DMFT calculation the magnetic moment was forced to be zero in a second calculation, so all magnetic effects can be included on DMFT level. On this forced zero magnetic moment calculation dmftproj was employed to calculated the localized Wannier orbitals for the DMFT calculation. As this forced zero moment calculation is basically paramagnetic, the projection was done exactly like in section 4.1 - the only difference being that one ends up with two impurities for the two (magnetically) inequivalent sites.

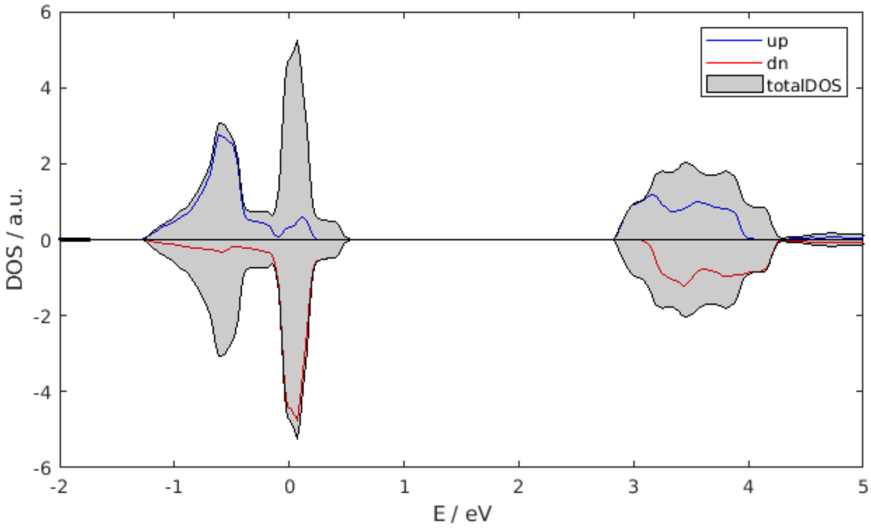

Figure 4.11 – Spin-resolved DFT-DOS of anti-ferromagnetic BYIO.

4.2.3 DMFT

As introduced in section 3.2.6 it is sufficient to solve the impurity problem for one site, as long as one finds a transformation between the two (magnetically) inequivalent sites. For BYIO this transformation was found by looking at the two site's $G_{\text{loc}}(i\omega_n)$s, resulting in the simple transformation matrix (acting on the $t_{2\mathrm{g}}$ manifold):

$$T = \begin{bmatrix} -1 & 0 & 0 & 0 & 0 & 0 \\ 0 & 1 & 0 & 0 & 0 & 0 \\ 0 & 0 & -1 & 0 & 0 & 0 \\ 0 & 0 & 0 & -1 & 0 & 0 \\ 0 & 0 & 0 & 0 & 1 & 0 \\ 0 & 0 & 0 & 0 & 0 & -1 \end{bmatrix} \tag{4.3}$$

Together with the spin-flip matrix from equation (3.18) the DMFT loop introduced in Fig. 3.2 can be implemented and performed. However, the used CTHYB solver limits the temperature range to finite, not-too-low temperatures. The calculations were performed in a range of 100 − 290 K ($\beta = 120 - 40$ eV^{-1}). A plot of the densities in cubic basis over the iterations can be found in Fig. 4.12.

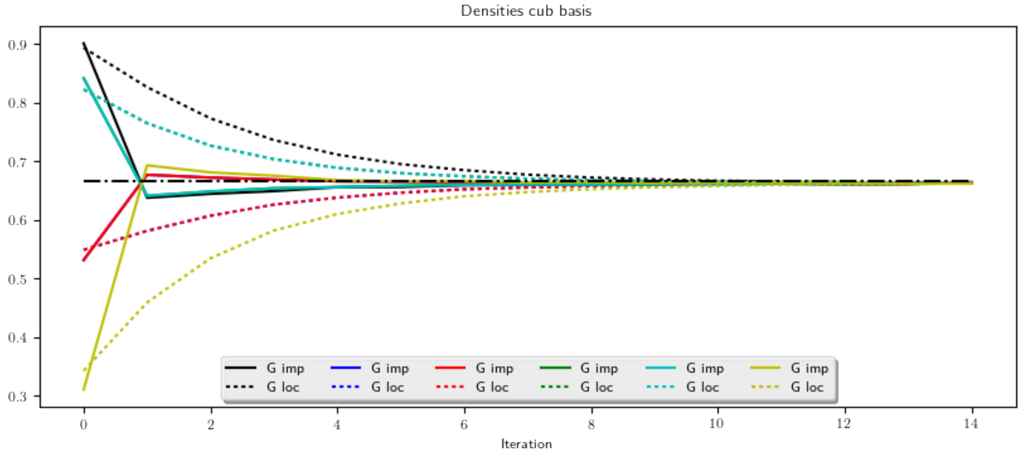

Figure 4.12 – Densities in cubic basis over the iteration. The calculation starts initialized in a anti-ferromagnetic state, however it goes to paramagnetic almost immediately. The dashed lines represent the densities from the local Green's functions, the slower convergence compared to the densities of the impurity's Green's functions comes from mixing.
The calculation was performed at $\beta = 40$ eV^{-1} (≈ 290 K).

Looking at Fig. 4.12 it is obvious that the anti-ferromagnetic state is not achieved for $\beta = 40$ eV^{-1}. The result does not change down to $\beta = 120$ eV^{-1} ($\approx$ 100 K). Of course we are still (far) away from the proposed transition temperature of 1.7 K [11] and it is no big surprise that the material goes into a paramagnetic state at these temperatures.

4.3 Summary and Outlook

Paramagnetic system: The paramagnetic calculation (section 4.1) clearly confirms the breakdown of the $J_{\text{eff}} = 0$ picture for Ba$_2$YIrO$_6$. The reason for this seems to be combination of band-structure effect and small enough SOC, leading to a overlap of the $J_{\text{eff}} = 1/2$ and $J_{\text{eff}} = 3/2$ bands in the DFT results (see Fig. 4.2b and 4.8). The addition of an interaction $U = 2$ eV then leads to Mott transitions in both bands, resulting in an insulating state with some electrons remaining in the $J_{\text{eff}} = 1/2$ lower Hubbard-band (below the Fermi level).

One possible further research topic would be to introduce the SOC not on DFT level, but in form of a $\zeta \boldsymbol{L} \cdot \boldsymbol{S}$ term in the interaction Hamiltonian. Thus it would be possible to tweak the value of ζ and to investigate its influence on the magnetic behaviour.

Anti-ferromagnetic system: The anti-ferromagnetic calculations (section 4.2) showed an absence of long-range ordering down to 100 K. However, this is not surprising, considering we are still far above the proposed transition temperature of 1.7 K [11]. Further research with a different solver (e.g. a MPS $T = 0$ K solver [55]) needs to be done to make a convincing argument for or against long-range ordering in Ba$_2$YIrO$_6$.

Sr$_2$YIrO$_6$: The framework laid out in this thesis might also be applied to Sr$_2$YIrO$_6$, thus investigating the influence of non-cubic crystal fields on the magnetic behaviour of Iridium double perovskites.

Listings

3.1 Generation of HDF archive 36
3.2 Calculating the DOS in Wannier basis 36
3.3 Finding the block structure in SumkDFT 39
3.4 Picking only t2g orbitals in SumkDFT 39
3.5 Diagonalizing Hloc 40
3.6 Transformation of U matrix 40
3.7 Transformation of Green's functions 41
3.8 Transformation of operators 41
3.10 "Hermitian Symmetrization" of Sigma 41
3.9 transform_operator() method 42
3.11 Measurement of density matrix and exp. values in CTHYB . . 44
3.12 L operator via T-P equivalence 45
3.13 L operator with removed eg orbitals 45
3.14 remove_all_eg_operators() method 46
3.15 S operator 47

List of Figures

1.1 Energy splittings of d-orbitals 2
1.2 Double perovskite crystal structure of BYIO 3

2.1 Perovskite crystal structure 6
2.2 Crystal-field splitting of d orbitals under octahedral crystal field 7
2.3 DFT loop 20
2.4 Mean field loop 22
2.5 Mapping of a lattice problem onto an impurity problem 23
2.6 DMFT loop 26

3.1 DMFT loop in TRIQS 43
3.2 AFM DMFT loop in TRIQS 49

4.1 Double perovskite crystal structure of BYIO 52
4.2 DFT band structure for BYIO 53
4.3 DFT orbital character plot for BYIO 54
4.4 DOS of BYIO in Wannier basis 55
4.5 $G_{\mathrm{loc}}(\omega)$ of BYIO 57
4.6 Hybridisation function $\Delta(\omega)$ of BYIO 58
4.7 Metal-Insulator transition in BYIO 59
4.8 Influence of the interaction parameter $U = 2$ on the spectral function 61
4.9 Influence of various interaction parameters on the spectral function 62
4.10 Anti-ferromagnetic configurations of fcc-like structures 63
4.11 Spin-resolved DFT-DOS of anti-ferromagnetic BYIO. 64
4.12 Densities in cubic basis over the iteration 65

List of Tables

2.1 Comparison between DMFT, MFT and DFT 25

4.1 Magnetic moment of BYIO in DFT 52
4.2 Expectation values of angular momenta for BYIO 60
4.3 Temperature dependence of $\langle J^2 \rangle$ in DMFT 60
4.4 U-dependence of $\langle J^2 \rangle$ and densities 61

Bibliography

[1] N. Mott, "Metal-insulator transition," *Reviews of Modern Physics*, vol. 40, no. 4, p. 677, 1968. (Cit. on p. 1.)

[2] G. Grüner, "The dynamics of charge-density waves," *Rev. Mod. Phys.*, vol. 60, pp. 1129–1181, Oct 1988. (Cit. on p. 1.)

[3] J. G. Bednorz and K. A. Müller, "Possible high t_c superconductivity in the Ba-La-Cu-O system," *Zeitschrift für Physik B Condensed Matter*, vol. 64, no. 2, pp. 189–193, 1986. (Cit. on p. 1.)

[4] B. Kim, H. Jin, S. Moon, J.-Y. Kim, B.-G. Park, C. Leem, J. Yu, T. Noh, C. Kim, S.-J. Oh, *et al.*, "Novel $j_{\text{eff}} = 1/2$ mott state induced by relativistic spin-orbit coupling in Sr_2IrO_4," *Physical review letters*, vol. 101, no. 7, p. 076402, 2008. (Cit. on pp. 1 and 2.)

[5] T. Dey, A. Maljuk, D. Efremov, O. Kataeva, S. Gass, C. Blum, F. Steckel, D. Gruner, T. Ritschel, A. Wolter, *et al.*, "Ba_2YIrO_6: a cubic double perovskite material with Ir 5+ ions," *Physical Review B*, vol. 93, no. 1, p. 014434, 2016. (Cit. on pp. 2, 3, and 63.)

[6] M. Bremholm, S. Dutton, P. Stephens, and R. Cava, "$NaIrO_3$ —a pentavalent post-perovskite," *Journal of Solid State Chemistry*, vol. 184, no. 3, pp. 601 – 607, 2011. (Cit. on p. 2.)

[7] L. Du, X. Sheng, H. Weng, and X. Dai, "The electronic structure of $NaIrO_3$, mott insulator or band insulator?," *EPL (Europhysics Letters)*, vol. 101, no. 2, p. 27003, 2013. (Cit. on p. 2.)

[8] G. Cao, T. Qi, L. Li, J. Terzic, S. Yuan, L. E. DeLong, G. Murthy, and R. K. Kaul, "Novel Magnetism of Ir 5+ Ions in the Double Perovskite Sr_2YIrO_6," *Physical review letters*, vol. 112, no. 5, p. 056402, 2014. (Cit. on pp. 2 and 3.)

[9] B. Ranjbar, E. Reynolds, P. Kayser, B. J. Kennedy, J. R. Hester, and J. A. Kimpton, "Structural and magnetic properties of the iridium double perovskites $\mathrm{Ba_{2-x}Sr_xYIrO_6}$," *Inorganic Chemistry*, vol. 54, no. 21, pp. 10468–10476, 2015. PMID: 26488369. (Cit. on pp. 2 and 51.)

[10] A. Nag, S. Bhowal, A. Chakraborty, M. Sala, A. Efimenko, F. Bert, P. Biswas, A. Hillier, M. Itoh, S. Kaushik, *et al.*, "Origin of magnetic moments and presence of spin-orbit singlets in $\mathrm{Ba_2YIrO_6}$," *Physical Review B*, vol. 98, no. 1, p. 014431, 2018. (Cit. on p. 2.)

[11] J. Terzic, H. Zheng, F. Ye, H. Zhao, P. Schlottmann, L. E. De Long, S. Yuan, and G. Cao, "Evidence for a low-temperature magnetic ground state in double-perovskite iridates with Ir 5+ $5d^4$ ions," *Physical Review B*, vol. 96, no. 6, p. 064436, 2017. (Cit. on pp. 2, 3, 63, 65, and 66.)

[12] K. Pajskr, P. Novák, V. Pokorný, J. Kolorenč, R. Arita, and J. Kuneš, "On the possibility of excitonic magnetism in Ir double perovskites," *Physical Review B*, vol. 93, no. 3, p. 035129, 2016. (Cit. on pp. 2, 3, and 56.)

[13] S. Bhowal, S. Baidya, I. Dasgupta, and T. Saha-Dasgupta, "Breakdown of $j = 0$ nonmagnetic state in d^4 iridate double perovskites: A first-principles study," *Phys. Rev. B*, vol. 92, p. 121113, Sep 2015. (Cit. on pp. 2, 52, and 63.)

[14] S. Fuchs, T. Dey, G. Aslan-Cansever, A. Maljuk, S. Wurmehl, B. Büchner, and V. Kataev, "Unraveling the nature of magnetism of the $5d^4$ double perovskite $\mathrm{Ba_2YIrO_6}$," *Physical review letters*, vol. 120, no. 23, p. 237204, 2018. (Cit. on p. 2.)

[15] G. Khaliullin, "Excitonic magnetism in Van Vleck-type d^4 Mott insulators," *Physical review letters*, vol. 111, no. 19, p. 197201, 2013. (Cit. on p. 3.)

[16] O. N. Meetei, W. S. Cole, M. Randeria, and N. Trivedi, "Novel magnetic state in d^4 Mott insulators," *Physical Review B*, vol. 91, no. 5, p. 054412, 2015. (Cit. on p. 3.)

[17] E. Pavarini, "Crystal-field theory, tight-binding method and jahn-teller effect," *Correlated electrons: from models to materials*, vol. 2, pp. 6–2, 2012. (Cit. on p. 7.)

[18] F. Schwabl, *Quantenmechanik (QM I): Eine Einführung.* Springer-Verlag, 2007. (Cit. on pp. 8 and 47.)

[19] F. Schwabl, *Quantenmechanik für Fortgeschrittene.* Springer, 1997. (Cit. on pp. 10, 11, and 12.)

[20] J. D. Bjorken and S. D. Drell, *Relativistic quantum mechanics.* McGraw-Hill, 1965. (Cit. on p. 11.)

[21] R. Triebl, *Interplay of spin-robit coupling and strong electronic correlations in multiorbitals systems and topological insulators.* PhD thesis, TU Graz, July 2018. (Cit. on p. 11.)

[22] G. Kraberger, *Development of a full matrix ab-initio scheme for materials with strong spin-orbit coupling and Coulomb interactions.* PhD thesis, TU Graz, February 2018. (Cit. on pp. 13, 38, 39, 56, and 59.)

[23] R. M. White and B. Bayne, *Quantum theory of magnetism*, vol. 1. Springer, 1983. (Cit. on pp. 14 and 15.)

[24] P. A. M. Dirac, *The principles of quantum mechanics.* Oxford university press, 1981. (Cit. on p. 15.)

[25] W. Nolting, *Grundkurs Theoretische Physik 7: Viel-Teilchen-Theorie.* Springer-Verlag, 2014. (Cit. on p. 16.)

[26] W. Kohn, "Nobel lecture: Electronic structure of matter - wave functions and density functionals," *Rev. Mod. Phys.*, vol. 71, pp. 1253–1266, Oct 1999. (Cit. on pp. 17 and 20.)

[27] P. Hohenberg and W. Kohn, "Inhomogeneous electron gas," *Phys. Rev.*, vol. 136, pp. B864–B871, Nov 1964. (Cit. on p. 18.)

[28] W. Kohn and L. J. Sham, "Self-consistent equations including exchange and correlation effects," *Physical review*, vol. 140, no. 4A, p. A1133, 1965. (Cit. on pp. 18 and 19.)

[29] J. P. Perdew, J. A. Chevary, S. H. Vosko, K. A. Jackson, M. R. Pederson, D. J. Singh, and C. Fiolhais, "Atoms, molecules, solids, and surfaces: Applications of the generalized gradient approximation for exchange and correlation," *Physical Review B*, vol. 46, no. 11, p. 6671, 1992. (Cit. on pp. 20 and 51.)

[30] A. Georges, G. Kotliar, W. Krauth, and M. J. Rozenberg, "Dynamical mean-field theory of strongly correlated fermion systems and the limit of infinite dimensions," *Reviews of Modern Physics*, vol. 68, no. 1, p. 13, 1996. (Cit. on p. 21.)

[31] A. Georges, “Strongly correlated electron materials: Dynamical mean-field theory and electronic structure,” in *AIP Conference Proceedings*, vol. 715, pp. 3–74, AIP, 2004. (Cit. on pp. 21, 22, 23, 25, and 27.)

[32] A. Georges, *Exact Functionals, Effective Actions and (Dynamical) Mean-Field Theories: Some Remarks*, pp. 375–394. Dordrecht: Springer Netherlands, 2002. (Cit. on p. 25.)

[33] W. Metzner and D. Vollhardt, “Correlated lattice fermions in d=∞ dimensions,” *Physical review letters*, vol. 62, no. 3, p. 324, 1989. (Cit. on p. 27.)

[34] E. Gull, A. J. Millis, A. I. Lichtenstein, A. N. Rubtsov, M. Troyer, and P. Werner, “Continuous-time monte carlo methods for quantum impurity models,” *Reviews of modern physics*, vol. 83, no. 2, p. 349, 2011. (Cit. on p. 27.)

[35] J. E. Hirsch and R. M. Fye, “Monte carlo method for magnetic impurities in metals,” *Physical review letters*, vol. 56, no. 23, p. 2521, 1986. (Cit. on p. 27.)

[36] P. Seth, I. Krivenko, M. Ferrero, and O. Parcollet, “TRIQS/CTHYB: A continuous-time quantum monte carlo hybridisation expansion solver for quantum impurity problems,” *Computer Physics Communications*, vol. 200, pp. 274–284, 2016. (Cit. on pp. 28 and 35.)

[37] E. Loh Jr, J. Gubernatis, R. Scalettar, S. White, D. Scalapino, and R. Sugar, “Sign problem in the numerical simulation of many-electron systems,” *Physical Review B*, vol. 41, no. 13, p. 9301, 1990. (Cit. on p. 28.)

[38] M. Troyer and U.-J. Wiese, “Computational complexity and fundamental limitations to fermionic quantum monte carlo simulations,” *Physical review letters*, vol. 94, no. 17, p. 170201, 2005. (Cit. on p. 28.)

[39] S. Chandrasekharan and U.-J. Wiese, “Meron-cluster solution of fermion sign problems,” *Physical Review Letters*, vol. 83, no. 16, p. 3116, 1999. (Cit. on p. 28.)

[40] C. Martins, *Interplay of Spin-Orbit Coupling and Electronic Coulomb Interactions in Strontium Iridate* Sr_2IrO_4. PhD thesis, Ecole Polytechnique X, 2010. (Cit. on pp. 29 and 31.)

[41] V. Vildosola, L. Pourovskii, C. Martins, and M. Aichhorn, “Introduction to dmftproj.” `https://triqs.github.io/dft_tools/master/`

`_downloads/TutorialDmftproj.pdf`. Accessed: 2019-02-26. (Cit. on pp. 30 and 34.)

[42] M. Karolak, G. Ulm, T. Wehling, V. Mazurenko, A. Poteryaev, and A. Lichtenstein, "Double counting in LDA+DMFT—the example of NiO," *Journal of Electron Spectroscopy and Related Phenomena*, vol. 181, no. 1, pp. 11 – 15, 2010. Proceedings of International Workshop on Strong Correlations and Angle-Resolved Photoemission Spectroscopy 2009. (Cit. on p. 30.)

[43] M. Aichhorn, L. Pourovskii, P. Seth, V. Vildosola, M. Zingl, O. E. Peil, X. Deng, J. Mravlje, G. J. Kraberger, C. Martins, M. Ferrero, and O. Parcollet, "TRIQS/DFTTools: A TRIQS application for ab initio calculations of correlated materials," *Computer Physics Communications*, vol. 204, pp. 200 – 208, 2016. (Cit. on pp. 30, 31, 35, and 36.)

[44] V. I. Anisimov, F. Aryasetiawan, and A. Lichtenstein, "First-principles calculations of the electronic structure and spectra of strongly correlated systems: the LDA+U method," *Journal of Physics: Condensed Matter*, vol. 9, no. 4, p. 767, 1997. (Cit. on p. 31.)

[45] E. Pavarini, E. Koch, D. Vollhardt, and A. I. Lichtenstein, *DMFT at 25: infinite dimensions: lecture notes of the Autumn School on Correlated Electrons 2014: at Forschungszentrum Jülich 15-19 September 2014*. Forschungszentrum Jülich, Zentralbibliothek, Verl., 2014. (Cit. on p. 31.)

[46] V. I. Anisimov, J. Zaanen, and O. K. Andersen, "Band theory and Mott insulators: Hubbard U instead of Stoner I," *Phys. Rev. B*, vol. 44, pp. 943–954, Jul 1991. (Cit. on p. 31.)

[47] K. Held, "Electronic structure calculations using dynamical mean field theory," *Advances in physics*, vol. 56, no. 6, pp. 829–926, 2007. (Cit. on p. 31.)

[48] K. Schwarz, P. Blaha, and G. K. Madsen, "Electronic structure calculations of solids using the WIEN2k package for material sciences," *Computer Physics Communications*, vol. 147, no. 1-2, pp. 71–76, 2002. (Cit. on pp. 33 and 51.)

[49] X. Rocquefelte, "Relativistic effects and non-collinear magnetism," *20th WIEN2k Workshop*, 2013. (Cit. on p. 34.)

[50] P. Novak, “Calulation of spin-orbit coupling.” `http://susi.theochem.tuwien.ac.at/reg_user/textbooks/novak_lecture_on_spinorbit.pdf`. Accessed: 2019-02-26. (Cit. on p. 34.)

[51] O. Parcollet, M. Ferrero, T. Ayral, H. Hafermann, I. Krivenko, L. Messio, and P. Seth, “TRIQS: A toolbox for research on interacting quantum systems,” *Computer Physics Communications*, vol. 196, pp. 398–415, 2015. (Cit. on pp. 34 and 36.)

[52] G. J. Kraberger, R. Triebl, M. Zingl, and M. Aichhorn, “Maximum entropy formalism for the analytic continuation of matrix-valued green’s functions,” *Phys. Rev. B*, vol. 96, p. 155128, Oct 2017. (Cit. on pp. 35 and 61.)

[53] G. Kraberger, “Projectors with two impurities,” March 2018. (Cit. on p. 48.)

[54] J. E. Gubernatis, M. Jarrell, R. N. Silver, and D. S. Sivia, “Quantum monte carlo simulations and maximum entropy: Dynamics from imaginary-time data,” *Phys. Rev. B*, vol. 44, pp. 6011–6029, Sep 1991. (Cit. on p. 61.)

[55] D. Bauernfeind, M. Zingl, R. Triebl, M. Aichhorn, and H. G. Evertz, “Fork tensor-product states: efficient multiorbital real-time dmft solver,” *Physical Review X*, vol. 7, no. 3, p. 031013, 2017. (Cit. on p. 66.)